Research Square

Preprints are preliminary reports that have not undergone peer review.
They should not be considered conclusive, used to inform clinical practice,
or referenced by the media as validated information.

Contextual gating modifies climate-conditioned dengue transmission potential across India

Subrahmanya Hari Prasad Peri

pshari19@gmail.com

IIT Kharagpur https://orcid.org/0000-0002-8182-7661

ANV Satyanarayana

IIT Kharagpur

Article

Keywords:

Posted Date: October 29th, 2026

DOI: https://doi.org/10.21203/rs.3.rs-11523748/v1

License: This work is licensed under a Creative Commons Attribution 4.0 International License.
Read Full License

Additional Declarations: There is **NO** Competing Interest.

Contextual gating modifies climate-conditioned dengue transmission potential across India

Peri Subrahmanya Hari Prasad[1,*] and **A. N. V. Satyanarayana**[1]

[1]Centre for Oceans, Rivers, Atmosphere and Land Sciences (CORAL), Indian Institute of Technology Kharagpur, Kharagpur 721302, West Bengal, India

[*]Correspondence: pshari19@gmail.com

Abstract

Climatic conditions shape dengue transmission potential, but ecological occurrence and settlement characteristics may alter its geographical expression. Here, we use CliMed, a daily mechanistic framework driven by median climate forcing from three CMIP6 models, to investigate dengue transmission potential across India under historical (2005–2014) and near-term (2026–2035) conditions across three Shared Socioeconomic Pathways. Spatially averaged entomological inoculation rate (EIR) increased by 13.8–17.8% across scenarios, while high-transmission hotspots remained geographically consistent with historical conditions (Jaccard similarity: 0.885–0.897). Under identical SSP2-4.5 forcing, full contextual gating reduced mean EIR by 83.4% and substantially reorganised hotspot geography (Jaccard similarity: 0.301). Persistent hotspots exhibited comparable geographical reclassification (Jaccard similarity: 0.272), despite largely conserved seasonal timing. These findings distinguish climatic intensification from context-dependent geographical prioritisation and temporal persistence, providing a mechanistic basis for understanding the spatial and temporal organisation of climate-sensitive dengue transmission potential.

Keywords: Dengue; climate variability; mechanistic modeling; contextual gating; spatial heterogeneity; transmission potential; vector occurrence; CMIP6

Introduction

Dengue transmission is shaped by interacting climatic, ecological and human-environmental processes, making its geographical distribution and seasonal dynamics particularly sensitive to environmental variability[1–3]. Temperature influences mosquito development, survival, biting activity and viral incubation, while precipitation and atmospheric moisture modify the environmental conditions supporting vector populations and transmission[4,5]. Global modelling studies have demonstrated that changes in climatic conditions can substantially redistribute areas suitable for Aedes-borne virus transmission, with geographically heterogeneous responses to warming and associated changes in the distribution of populations potentially exposed to dengue[6–8]. However, the geographical expression of transmission potential depends on more than climatic suitability. Vector occurrence, habitat characteristics, settlement patterns and human-associated environmental conditions influence where favourable climatic conditions coincide with the ecological and contextual requirements for transmission[9,10].

Mechanistic modelling provides a means of translating climatic variability into biologically interpretable transmission processes, rather than relying exclusively on statistical associations between environmental conditions and disease occurrence[11]. Experimental and theoretical investigations have demonstrated that mosquito development, survival, biting frequency, vector competence and viral incubation respond nonlinearly to temperature, with daily thermal fluctuations further modifying transmission-related biological processes[4,12–14]. Precipitation and atmospheric moisture additionally influence mosquito habitats, adult-vector survival and population dynamics, creating interactions between climatic conditions and local environmental characteristics[3]. Building on these biological relationships, trait-based and spatially explicit mechanistic frameworks have been developed to investigate the geographical and temporal variability of mosquito-borne disease dynamics and arboviral transmission potential[5,15]. Such approaches allow climatic forcing to be propagated through interacting vector and transmission processes, providing a basis for estimating quantities such as the entomological inoculation rate (EIR) and force of infection (FOI)[16]. Importantly, the resulting transmission landscapes reflect the combined responses of multiple biological processes operating over different timescales, making the representation of daily climatic variability and environmental heterogeneity central to interpreting their spatial and seasonal behaviour.

Recent advances in dengue and vector-distribution modelling have increasingly recognised that climatic suitability must be interpreted alongside ecological conditions and human-associated environmental characteristics. Studies in Vietnam have demonstrated that climate, urban infrastructure and human mobility contribute differently to dengue emergence, while broader investigations have shown that environmental barriers and human connectivity influence the geographical processes underlying transmission[9,10]. Similarly, climate- and population-dependent diffusion modelling has highlighted how vector establishment and geographical expansion depend on processes extending beyond environmental suitability alone[17]. These developments establish the importance of integrating multiple environmental and contextual dimensions, but also raise a complementary question: how do ecological occurrence and settlement-related constraints modify the intensity, geographical prioritisation and temporal persistence of transmission potential generated by a common mechanistic framework? Addressing this question requires distinguishing changes associated with climatic forcing from those arising through contextual constraints, while examining whether geographically persistent transmission hotspots remain similarly prioritised across alternative climate scenarios and environmental configurations.

India provides a particularly relevant setting for examining these interactions because its climatic diversity, pronounced monsoon seasonality, heterogeneous landscapes and contrasting settlement characteristics create substantial geographical variation in the environmental conditions supporting dengue transmission. Epidemiological investigations have documented the widespread occurrence of dengue across India, while systematic reviews and population-based serosurveys have revealed considerable regional heterogeneity in infection exposure[18–20]. Climatic analyses have further highlighted the influence of temperature, precipitation and seasonal variability on dengue dynamics, with differing relationships across geographical and climatic regions[21]. At finer spatial scales, investigations in Delhi have demonstrated pronounced geographical clustering and seasonal variation in dengue occurrence[22].

Here, we present CliMed, a spatially explicit mechanistic modelling framework that integrates climate-sensitive vector biology, land-use characteristics and coupled vector–host transmission processes to investigate the geographical and temporal variability of dengue transmission potential across India. Using daily climate forcing constructed from three CMIP6 Earth system models, we compare historical conditions (2005–2014) with near-term projections (2026–2035) under SSP1-2.6, SSP2-4.5 and SSP5-8.5. We first examine changes in entomological inoculation rate (EIR) and force of infection (FOI), including their nonlinear climatic relationships, seasonal characteristics and geographical hotspot distributions. We then evaluate the consistency of transmission hotspots across climate scenarios and compare vector-occurrence, VIIRS and full contextual gating under common SSP2-4.5 forcing to quantify changes in transmission intensity and geographical prioritisation. Finally, we assess the temporal recurrence of high-transmission locations and the sensitivity of persistent-hotspot classifications to alternative thresholds. By distinguishing climatic intensification, contextual geographical reorganisation and temporal hotspot persistence within a common mechanistic framework, this study provides an integrated perspective on how climatic and environmental heterogeneity shapes dengue transmission potential and offers a basis for identifying geographically consistent priorities for further ecological investigation.

Results

Spatial intensification and heterogeneous redistribution of mechanistic transmission potential

CliMed simulations revealed a spatially heterogeneous distribution of dengue transmission potential across India under historical (2005–2014) and near-term (2026–2035) climate conditions (Fig. 1). Using daily climate forcing derived from the median of three CMIP6 models, the grid-cell-averaged entomological inoculation rate (EIR) increased from 0.0591 infectious bites person^{-1} day^{-1} during the historical period to 0.0697 infectious bites person^{-1} day^{-1} under SSP2-4.5, representing an absolute increase of 0.0105 infectious bites person^{-1} day^{-1} (17.8%). The corresponding force of infection (FOI) increased from 0.0207 to 0.0244 day^{-1}, an absolute increase of 0.00369 day^{-1} (17.8%; Fig. 1d–f). Both periods exhibited pronounced geographical contrasts, with relatively high transmission potential concentrated in parts of northeastern India

and more localized areas of central, eastern and peninsular India, whereas much of northwestern India and the Himalayan region exhibited comparatively low values (Fig. 1a,b,d,e).

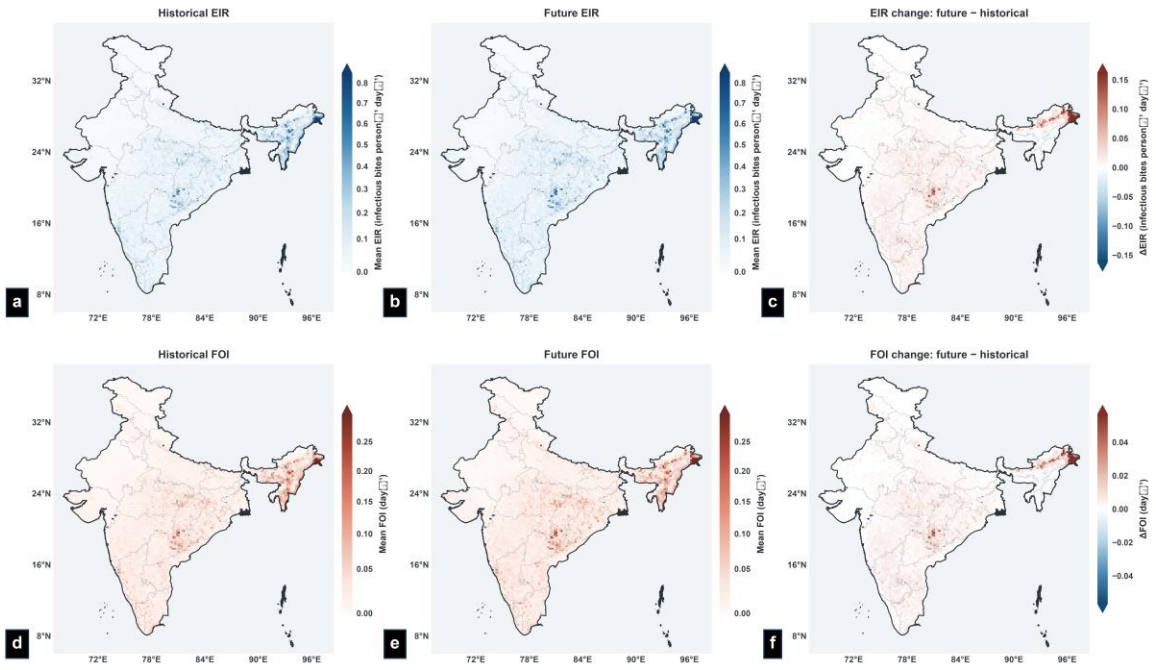


Figure 1 Spatial distribution and near-term intensification of mechanistic dengue transmission potential across India under three-GCM median climate forcing. *a,b, Mean entomological inoculation rate (EIR; infectious bites person⁻¹ day⁻¹) during the historical (2005–2014) and near-term (2026–2035) periods, respectively. c, Spatial change in mean EIR, calculated as near-term minus historical EIR. d,e, Mean force of infection (FOI; day⁻¹) during the corresponding historical and near-term periods, respectively. f, Spatial change in mean FOI, calculated as near-term minus historical FOI. Daily meteorological forcing was constructed from the median of three CMIP6 global climate models (MPI-ESM1-2-LR, MRI-ESM2-0 and ACCESS-ESM1-5), followed by mechanistic CliMed simulations on a common 20-km grid. The near-term experiment represents SSP2-4.5, with optional contextual gates disabled in both periods. Historical and near-term maps share identical colour scales within each transmission metric, while difference maps use symmetric, zero-centred scales, with red indicating increased and blue indicating decreased transmission potential. Across 8,292 common valid grid cells, mean EIR and FOI increased by 17.8%, with positive changes in 84.0% of cells. Colour scales are truncated at predefined upper percentiles for visualisation, whereas the reported statistics are calculated from the untruncated model outputs. EIR and FOI represent mechanistically simulated transmission potential rather than observed dengue incidence, and the period differences are not interpreted as formal attribution to anthropogenic climate change.*

Although the broad geographical structure of transmission potential remained similar between periods, the magnitude and spatial distribution of change were distinctly heterogeneous (Fig. 1c,f). Across 8,292 grid cells with valid estimates in both periods, EIR increased in 84.0% of cells, decreased in 8.3% and remained unchanged in 7.7%. The median cellwise EIR change was +0.00496 infectious bites person^{-1} day^{-1}, compared with a mean increase of +0.0105, indicating that larger localized increases contributed disproportionately to the spatially averaged change. Localized decreases occurred within the broader pattern of intensification.

Nonlinear climatic responses and limited explanatory performance for spatial changes in transmission potential

The climatic structure of mechanistic transmission potential was examined using near-surface air temperature, relative humidity and precipitation across 8,292 valid grid cells under historical and near-term conditions (Fig. 2a–c). Fitted conditional relationships showed pronounced nonlinearity across all three meteorological variables. EIR remained low under cooler temperature conditions and increased sharply towards the warmer end of the sampled distribution (Fig. 2a). Relative humidity exhibited a more gradual response, with increasing fitted EIR across intermediate humidity levels and a tendency towards saturation at higher values (Fig. 2b). Precipitation showed a non-monotonic fitted relationship, with EIR increasing towards intermediate rainfall conditions before declining at the wetter end of the distribution (Fig. 2c). Although the historical and near-term response curves retained broadly similar shapes, their magnitudes and local maxima differed.

The ability of annual-mean climatic changes to explain geographical variation in near-term EIR was evaluated using spatial-block cross-validation (Fig. 2d–f). The additive model incorporating changes in temperature, relative humidity and precipitation yielded a spatially cross-validated $R^2$of −0.071, indicating poorer predictive performance than a constant-mean reference. Removing individual predictors did not reduce predictive performance; instead, the cross-validated R^2increased by 0.0047 following temperature removal, 0.0098 following relative-humidity removal and 0.0318 following precipitation removal (Fig. 2d). The spline–ridge specification and spatial cross-validation settings are summarised in Supplementary Section S2 and Supplementary Table S1. The spatial distribution of the largest fitted local effects varied geographically, with different climatic variables contributing the greatest absolute fitted effects across different regions (Fig. 2e). However, the poor out-of-block predictive performance indicates that these local contributions should not be interpreted as independently established climatic drivers of EIR change. The residual distribution further revealed geographically structured discrepancies between simulated and statistically reconstructed ΔEIR, including pronounced differences in parts of northeastern India (Fig. 2f).

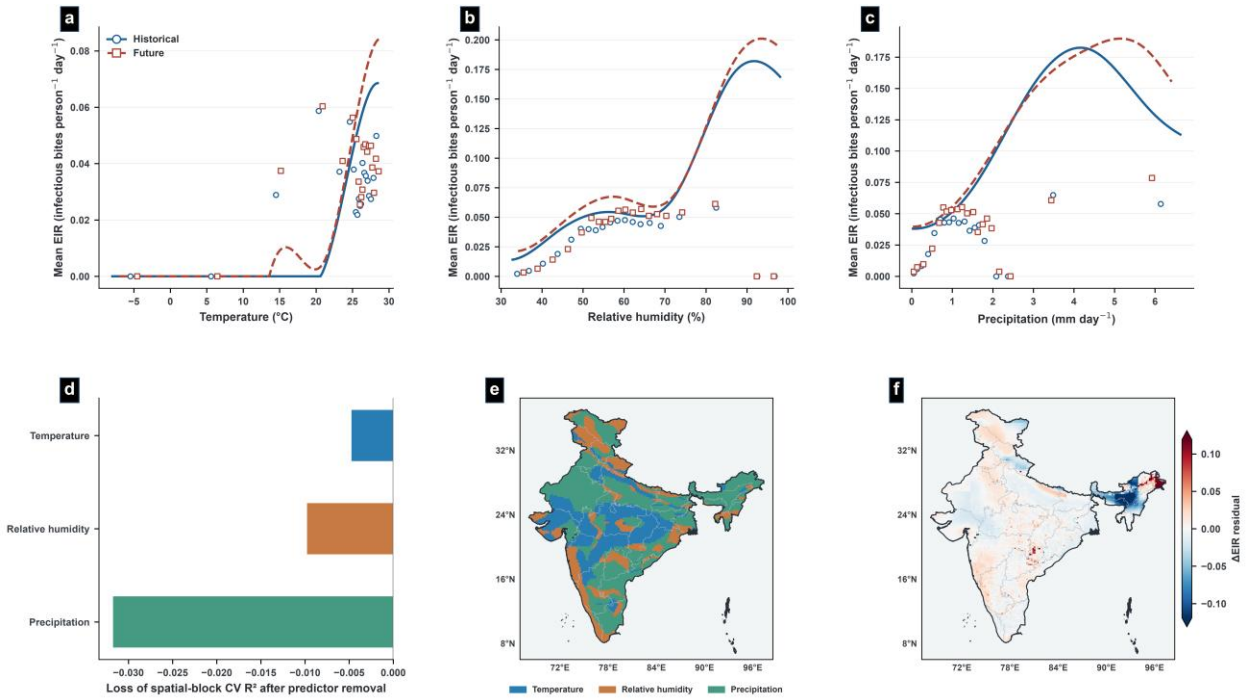


Figure 2 Nonlinear climatic relationships and spatial predictive performance of meteorological changes for mechanistic transmission potential across India. *Empirical and fitted relationships between entomological inoculation rate (EIR) and near-surface air temperature, relative humidity and precipitation, respectively, for the historical (2005–2014) and near-term (2026–2035; SSP2-4.5) periods. Open blue circles and red squares represent median EIR values within 20 empirical climate-quantile classes, while solid blue and dashed red curves represent fitted conditional responses from additive spline regression models. The fitted curves are evaluated by varying one meteorological variable while holding the remaining variables at their median values; they are therefore not direct fits to the marginal quantile medians. d, Change in spatial-block cross-validated R^2 following removal of each meteorological predictor from the additive model of near-term-minus-historical EIR (ΔEIR). Negative values indicate that removing the predictor improved predictive performance. e, Spatial distribution of the meteorological variable with the largest absolute centred fitted contribution to ΔEIR in the full-sample additive model. Colours distinguish temperature, relative humidity and precipitation and do not indicate causal dominance. f, Spatial residuals of the cross-validated ΔEIR model, calculated as mechanistically simulated minus statistically predicted EIR change. Positive values indicate statistical underprediction and negative values indicate overprediction. The regression and spatial attribution analyses are post hoc characterisations of CliMed outputs rather than independent validation of the mechanistic model. All experiments use three-GCM median climate forcing, a common 20-km model grid and neutral optional contextual gates.*

Seasonal intensification of mechanistic transmission potential under near-term climatic conditions

The monthly climatology revealed pronounced seasonality in mechanistic dengue transmission potential across India, with EIR and FOI concentrated predominantly during the southwest monsoon period under both historical (2005–2014) and near-term (2026–2035; SSP2-4.5) conditions (Fig. 3a,b). August EIR increased from 0.2364 to 0.2782 infectious bites person^{-1} day^{-1} (17.7%), while September exhibited a larger absolute increase of 0.0456 infectious bites person^{-1} day^{-1}, corresponding to a 32.8% increase from 0.1391 to 0.1847. Transmission potential also increased during June (15.8%), July (16.6%) and October (31.4%), whereas lower values were simulated during May (−15.7%) and November (−33.9%) relative to the historical climatology. FOI

followed the same seasonal pattern, increasing from 0.0827 to 0.0974 day^{-1} in August and from 0.0487 to 0.0646 day^{-1} in September, consistent with its proportional relationship to EIR in the model configuration.

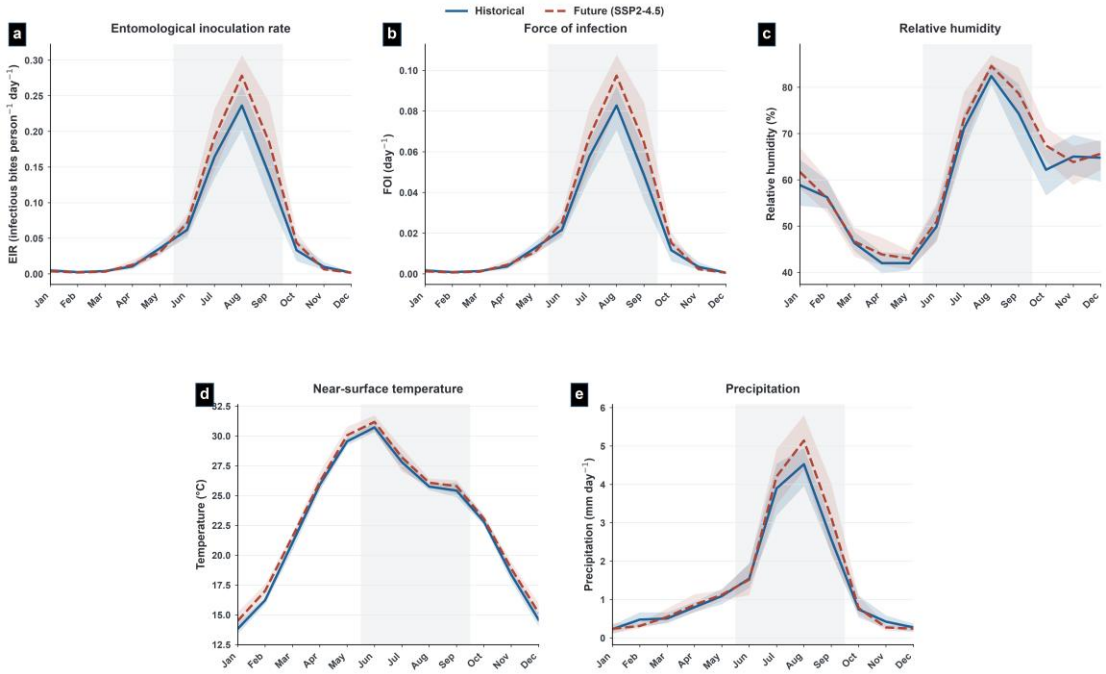


Figure 3 Historical and near-term monthly climatologies of mechanistic dengue transmission potential and meteorological forcing across India. *a,b, Monthly mean entomological inoculation rate (EIR; infectious bites person $^{-1}$ day $^{-1}$) and force of infection (FOI; day $^{-1}$), respectively, simulated by CliMed during historical (2005–2014) and near-term (2026–2035) periods. c–e, Corresponding monthly climatologies of relative humidity (%), near-surface air temperature (°C) and precipitation (mm day $^{-1}$), respectively. Solid blue lines represent historical conditions, while dashed red lines represent the near-term SSP2-4.5 experiment. Shaded envelopes indicate the 10th–90th percentile ranges calculated across ten year-specific monthly means, representing interannual variability rather than confidence intervals. The light-grey vertical shading denotes the June–September southwest monsoon period. Daily meteorological inputs were derived from three-GCM median climate forcing, and monthly climatologies were calculated by first averaging daily values within each calendar month and subsequently averaging the corresponding monthly values across ten years. Transmission outputs were evaluated on a common 20-km grid across India, with 8,292 common valid cells for EIR and FOI. All simulations were performed with optional occurrence and VIIRS contextual gates disabled. The figure characterises seasonal correspondence between climatic conditions and mechanistic transmission potential without implying direct statistical attribution of EIR or FOI changes to individual meteorological variables.*

The seasonal changes in simulated transmission potential occurred alongside differences in the meteorological forcing (Fig. 3c–e). Near-surface air temperature increased in every calendar month, with monthly mean differences ranging from approximately 0.23 to 0.78 °C. The highest climatological temperatures occurred in June, increasing from 30.71 °C historically to 31.17 °C under SSP2-4.5. Relative humidity exhibited a pronounced monsoon maximum in August, increasing from 82.44% to 84.63%, followed by larger absolute increases during September (+4.35 percentage points) and October (+5.23 percentage points). Precipitation similarly reached its maximum in August, increasing from 4.53 to 5.14 mm day^{-1} (13.6%), while September precipitation increased from 2.57 to 3.14 mm day^{-1} (22.1%).

Spatial stability of peak transmission timing and regional changes in seasonal concentration

Despite the intensification of monsoon-associated transmission potential (Fig. 3), the geographical timing of maximum entomological inoculation rate (EIR) remained largely conserved between the historical (2005–2014) and near-term (2026–2035; SSP2-4.5) periods (Fig. 4a–c). August was the dominant peak-transmission month across much of India, accounting for 81.4% of the 7,634 paired grid cells with complete, positive monthly EIR climatologies during the historical period and 79.5% under near-term conditions. Comparison between periods showed that the peak EIR month remained unchanged in 83.0% of grid cells, shifted later in 11.1%, and shifted earlier in 5.9%. These changes were geographically clustered rather than uniformly distributed, with later peak months occurring in parts of central and southern India and earlier shifts in portions of western and northern India (Fig. 4c). The median cellwise peak-month shift was zero.

Changes in seasonal concentration were evaluated using L_{80}, defined as the shortest contiguous, cyclic sequence of calendar months accounting for at least 80% of the annual climatological EIR (Fig. 4d–f). Historical L_{80} averaged 2.960 months across the paired spatial domain, compared with 2.968 months under near-term conditions, corresponding to a mean increase of only 0.009 months. Seasonal concentration remained unchanged in 82.8% of grid cells, while L_{80} decreased in 8.0% and increased in 9.2%. Spatially, longer concentration windows were apparent in parts of southern and northeastern India, whereas shorter windows characterised much of the northern and central domain. Localized reductions in L_{80}, indicating greater concentration of annual transmission potential within fewer consecutive months, occurred in parts of western and southern India, while increases were distributed across portions of northern, central and eastern India. The limited overall change in L_{80}, together with the predominance of unchanged peak months, indicates that near-term intensification of simulated EIR occurs primarily within an established seasonal structure rather than through a widespread geographical shift or systematic extension of the transmission season. Definitions and supporting seasonal-timing and concentration statistics are provided in Supplementary Section S3 and Supplementary Table S2.

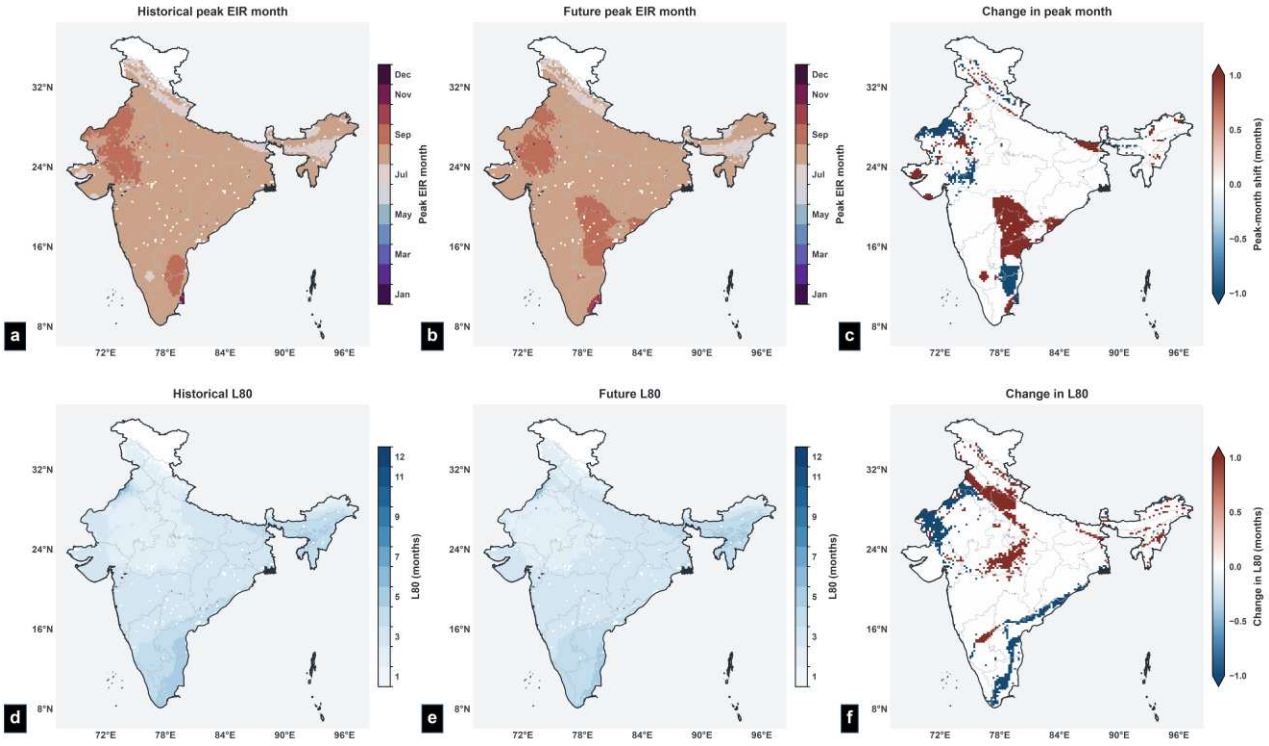


Figure 4 Spatial distribution and near-term changes in the timing and seasonal concentration of mechanistic dengue transmission potential across India. *a,b, Geographical distribution of the calendar month with maximum climatological entomological inoculation rate (EIR) during the historical (2005–2014) and near-term (2026–2035; SSP2-4.5) periods, respectively. The discrete colour scale represents January–December, allowing regional differences in peak-transmission timing to be distinguished. c, Change in peak EIR month between periods, calculated using the shortest signed displacement on a circular 12-month calendar. Positive values indicate later and negative values indicate earlier peak months. d,e, Spatial distribution of seasonal concentration* (L_{80}) *during the historical and near-term periods, respectively.* L_{80}*is the minimum number of consecutive calendar months required to account for at least 80% of annual climatological EIR, with temporal continuity evaluated across the December–January boundary. Smaller* L_{80}*values indicate greater seasonal concentration, whereas larger values indicate a broader distribution of annual transmission potential across the calendar year. f, Near-term-minus-historical change in* L_{80}*, where negative values indicate greater seasonal concentration and positive values indicate a broader seasonal window. Monthly EIR climatologies were calculated from daily CliMed outputs by averaging within each year-month and subsequently across the ten years in each period. The simulations used three-GCM median climate forcing, a common 20-km spatial grid and neutral optional contextual gates. Analyses were restricted to 7,634 grid cells with complete and positive monthly EIR climatologies in both periods. Difference-map colour limits were truncated for visualisation, while numerical statistics were calculated from the untruncated results. The indicators describe changes in simulated transmission seasonality rather than observed dengue incidence or formally attributed anthropogenic climate-change effects.*

Scenario-dependent intensification and geographical persistence of mechanistic transmission hotspots

Near-term projections under three CMIP6 Shared Socioeconomic Pathways (SSPs) revealed widespread increases in mechanistic dengue transmission potential across India, although the magnitude of change varied between scenarios (Fig. 5a–d). Relative to the historical period (2005–2014), the spatially averaged entomological inoculation rate (EIR) increased by 14.6% under SSP1-2.6, 17.8% under SSP2-4.5 and 13.8% under SSP5-8.5 during 2026–2035. The corresponding mean EIR increased from 0.0591 infectious bites person^{-1} day^{-1} historically to 0.0678, 0.0697 and 0.0673 infectious bites person^{-1} day^{-1}, respectively. Positive EIR changes occurred in 72.3%, 84.0% and 78.7% of the 8,292 common valid grid cells under SSP1-2.6, SSP2-4.5 and SSP5-8.5, respectively. Although SSP2-4.5 produced the largest spatially averaged

increase, the scenario ordering was non-monotonic, with SSP5-8.5 exhibiting a smaller increase than both SSP1-2.6 and SSP2-4.5 over the analysed near-term period.

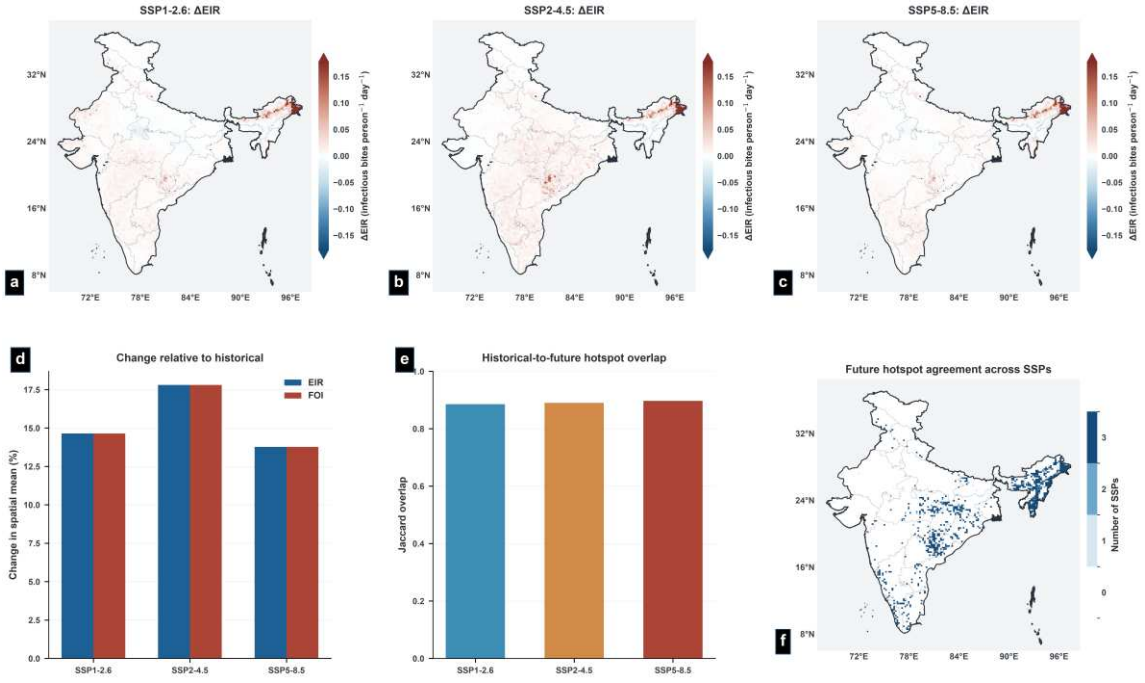


Figure 5 Near-term changes in mechanistic dengue transmission potential and spatial agreement of high-transmission hotspots across three CMIP6 climate scenarios. *a–c, Spatial changes in mean entomological inoculation rate (ΔEIR; infectious bites person⁻¹ day⁻¹) between the historical period (2005–2014) and near-term projections (2026–2035) under SSP1-2.6, SSP2-4.5 and SSP5-8.5, respectively. Changes were calculated as near-term minus historical mean EIR, with positive (red) and negative (blue) values displayed using a common symmetric, zero-centred colour scale. d, Percentage changes in spatially averaged EIR and force of infection (FOI) relative to the historical period across the three scenarios. Percentage changes represent the ratio of spatial means rather than averages of grid-cell percentage changes. e, Jaccard similarity coefficients quantifying the spatial overlap between historical and near-term EIR hotspots under each SSP, calculated as the number of grid cells classified as hotspots in both periods divided by the number classified in either period. f, Geographical agreement of future EIR hotspot classifications across the three SSPs. The discrete colour scale indicates whether each grid cell was classified as a future hotspot under zero, one, two or all three scenarios. Hotspots were defined as the upper 10% of strictly positive EIR values within each period or scenario, using a common spatial comparison domain. Daily meteorological forcing was constructed separately for each experiment using the median of three CMIP6 global climate models (MPI-ESM1-2-LR, MRI-ESM2-0 and ACCESS-ESM1-5), followed by one mechanistic CliMed simulation per period and scenario. All experiments used the common 20-km model grid, with optional vector-occurrence and VIIRS contextual gates disabled. Analyses included 8,292 common valid grid cells. Map colour limits were truncated at the 99.5th percentile of absolute EIR changes for visualisation, while numerical statistics were calculated from untruncated values. Hotspot agreement describes the consistency of relative modelled transmission-potential rankings and does not represent independent climate-model uncertainty, observed dengue incidence or validation against surveillance data.*

Despite differences in transmission intensity, the geographical distribution of high-EIR locations remained largely conserved across the three scenarios (Fig. 5e,f). Hotspots were defined separately within each experiment as the upper decile of grid cells with positive mean EIR. The historical-to-future Jaccard similarity coefficients were 0.885, 0.890 and 0.897 under SSP1-2.6, SSP2-4.5 and SSP5-8.5, respectively, indicating substantial overlap between historical and near-term hotspot distributions. Correspondingly, 94.0–94.6% of historical hotspot cells retained their hotspot classification under the future scenarios. Pairwise comparisons of future hotspot distributions yielded Jaccard coefficients ranging from 0.903 to 0.944. Of the 8,292 valid grid cells, 714 (8.61%) were classified as hotspots under all three SSPs, whereas 54 (0.65%) were classified under two scenarios and 45 (0.54%) under only one. Thus, approximately 93.3% of the 765

hotspot cells identified within each future scenario were shared across all three pathways. Scenario-level transmission and hotspot-agreement statistics are summarised in Supplementary Section S4 and Supplementary Table S3.

Ecological occurrence and settlement-related constraints attenuate transmission potential and reorganise spatial hotspot priorities

The influence of ecological occurrence and human-settlement-related constraints on mechanistic dengue transmission potential was investigated using four configurations under identical SSP2-4.5 climate forcing for 2026–2035: ungated, vector-occurrence gating, VIIRS gating and full gating (Fig. 6). The ungated simulation produced a spatially averaged entomological inoculation rate (EIR) of 0.0697 infectious bites person^{-1} day^{-1}, with pronounced spatial heterogeneity across northeastern, central and peninsular India (Fig. 6a). Introducing the vector-occurrence constraint reduced mean EIR to 0.0240 infectious bites person^{-1} day^{-1}, corresponding to a 65.6% attenuation relative to the ungated simulation (Fig. 6b). The VIIRS constraint produced a greater reduction, yielding a mean EIR of 0.0132 infectious bites person^{-1} day^{-1} (81.1% attenuation; Fig. 6c). Under full gating, mean EIR decreased further to 0.0116 infectious bites person^{-1} day^{-1}, representing an overall attenuation of 83.4% (Fig. 6d). Corresponding reductions in the spatially averaged force of infection (FOI) were 68.0%, 82.0% and 84.1% under vector-occurrence, VIIRS and full gating, respectively. Although mean transmission potential decreased substantially under all configurations, cellwise responses were not uniformly suppressive. Relative to the ungated simulation, EIR decreased in 84.7%, 88.0% and 88.6% of grid cells under the three respective configurations, while localized increases occurred in 7.2%, 3.9% and 3.3%. The geographical distribution of attenuation was similarly heterogeneous, with particularly pronounced reductions in northeastern India and additional spatially discontinuous reductions across central, eastern and southern regions (Fig. 6e).

Beyond reductions in absolute transmission intensity, the constraints substantially altered the geographical prioritisation of high-EIR locations (Fig. 6f). Hotspots were defined independently for each configuration as the upper 10% of grid cells with positive mean EIR. Relative to the ungated simulation, vector-occurrence gating retained 436 hotspot cells and reclassified 329, yielding a Jaccard similarity coefficient of 0.399. VIIRS gating retained 405 hotspot cells and reclassified 360 (Jaccard = 0.360), whereas full gating retained only 354 of the original 765 hotspot cells and introduced 411 newly prioritised cells (Jaccard = 0.301). Thus, 53.7% of ungated hotspot locations were no longer classified among the highest-EIR cells after full gating, despite the overall reduction in transmission potential.

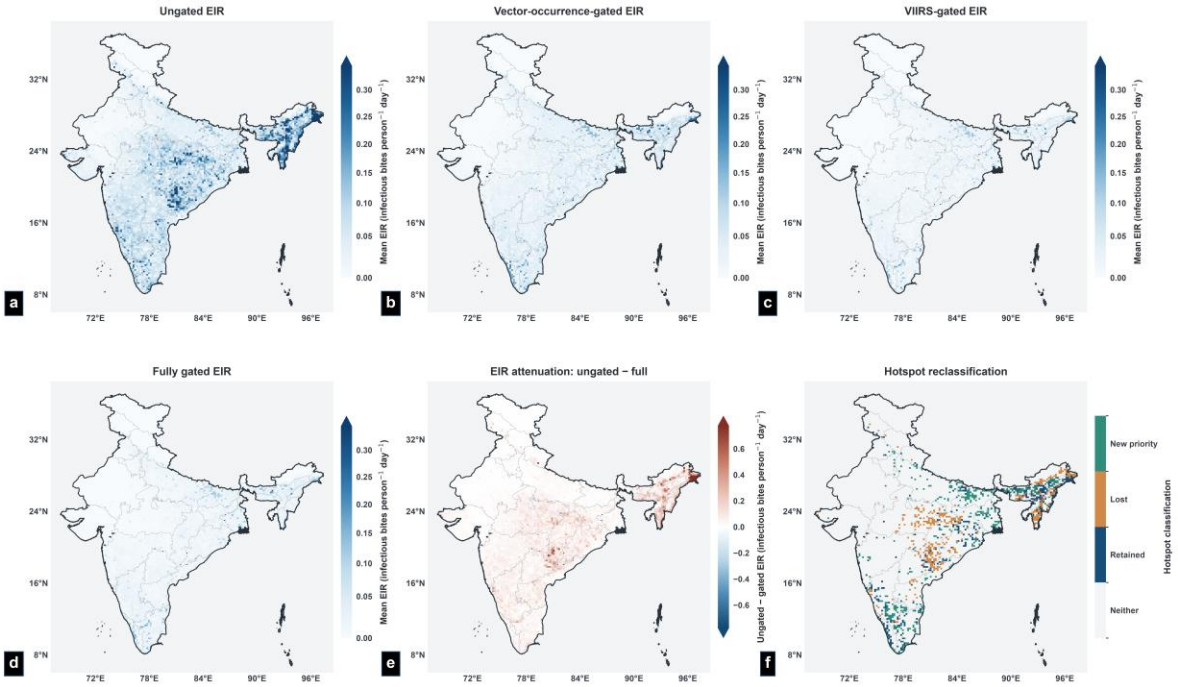


Figure 6 Effects of alternative contextual gating configurations on mechanistic dengue transmission potential and hotspot classification under SSP2-4.5. *a–d, Spatial distribution of mean entomological inoculation rate (EIR; infectious bites person⁻¹ day⁻¹) during 2026–2035 under four CliMed configurations: ungated (a), vector-occurrence gating alone (b), VIIRS gating alone (c) and full contextual gating (d). All configurations used the same three-GCM median SSP2-4.5 climate forcing and common 20-km model grid, allowing differences in transmission potential to be examined between the selected contextual configurations. A common colour scale was applied across panels a–d to facilitate direct comparison of transmission intensity. e, Spatial attenuation of EIR under full gating, calculated as ungated minus fully gated EIR. Positive values (red) indicate lower transmission potential after gating, whereas negative values (blue) indicate locally higher values under the fully gated configuration. f, Geographical reclassification of high-EIR hotspot cells between the ungated and fully gated configurations. Hotspots were independently defined as the upper 10% of strictly positive EIR values within each configuration. Dark blue indicates hotspot cells retained in both configurations, orange indicates locations classified as hotspots only in the ungated simulation, and green indicates locations newly classified as hotspots under full gating. Light-grey areas were not classified as hotspots in either configuration. All comparisons were performed over 8,292 common valid grid cells. Colour-scale limits for continuous transmission fields were truncated at the 99.5th percentile for visualisation, whereas reported statistics were calculated from untruncated model outputs. Vector occurrence and VIIRS were used as ecological and settlement-related contextual constraints, respectively; they do not directly represent future vector invasion, observed human mobility or reported dengue incidence. Changes in hotspot classification indicate relative spatial reprioritisation rather than necessarily increased absolute transmission potential.*

Grid-cell EIR rankings also changed, with Spearman rank correlations relative to the ungated simulation declining from 0.859 under vector-occurrence gating to 0.817 under VIIRS gating and 0.760 under full gating. These changes contrast with the substantially greater historical-to-future hotspot overlap observed across the three climate scenarios (Fig. 5), indicating that the tested contextual constraints produce more extensive relative spatial reorganisation than the differences among the near-term climate experiments.

The geographical reorganisation was also apparent when model outputs were aggregated to administrative units. State-mean EIR rankings changed substantially between ungated and fully gated configurations, with only five of the original ten highest-ranked states or union territories remaining in the top ten after full gating. Kerala increased from ninth to second position, Goa from eighteenth to third, Bihar from twenty-first to sixth and West Bengal from nineteenth to ninth,

whereas Arunachal Pradesh decreased from second to nineteenth and Chhattisgarh from eighth to twentieth. Andaman and Nicobar Islands retained the highest mean EIR ranking across all four configurations. These administrative comparisons provide an additional illustration of spatial reprioritisation, although individual state rankings are sensitive to the number and geographical distribution of contributing grid cells. The stronger mean attenuation under VIIRS gating and the additional reorganisation under full gating indicate that ecological occurrence and settlement-related information affect the geographical expression of mechanistic transmission potential differently, rather than functioning as interchangeable spatial filters. The complete contextual-configuration matrix, attenuation statistics and administrative rankings are provided in Supplementary Section S5, Supplementary Tables S4–S5 and Supplementary Fig. S1.

Temporal persistence and geographical reprioritisation of transmission hotspots under ecological and settlement-related constraints

The temporal stability of mechanistic dengue transmission hotspots was evaluated across the ten-year SSP2-4.5 simulation period (2026–2035) to determine whether ecological occurrence and settlement-related constraints altered not only the geographical distribution of transmission potential but also the recurrence of high-EIR locations (Fig. 7). Hotspots were identified independently within each configuration as the upper 10% of grid cells with positive annual entomological inoculation rate (EIR), and persistent hotspots were defined as locations retaining this classification for at least eight of the ten years. Under the ungated configuration, 645 of the 8,292 valid grid cells (7.78%) satisfied the persistence criterion, including 526 cells classified as hotspots in all ten years (Fig. 7a). After full contextual gating, 605 grid cells (7.30%) remained classified as persistent hotspots, of which 469 retained their annual hotspot classification throughout the entire decade (Fig. 7b). Although the total number of persistent hotspots changed relatively little, their geographical composition differed substantially between the ungated and fully gated configurations (Fig. 7c).

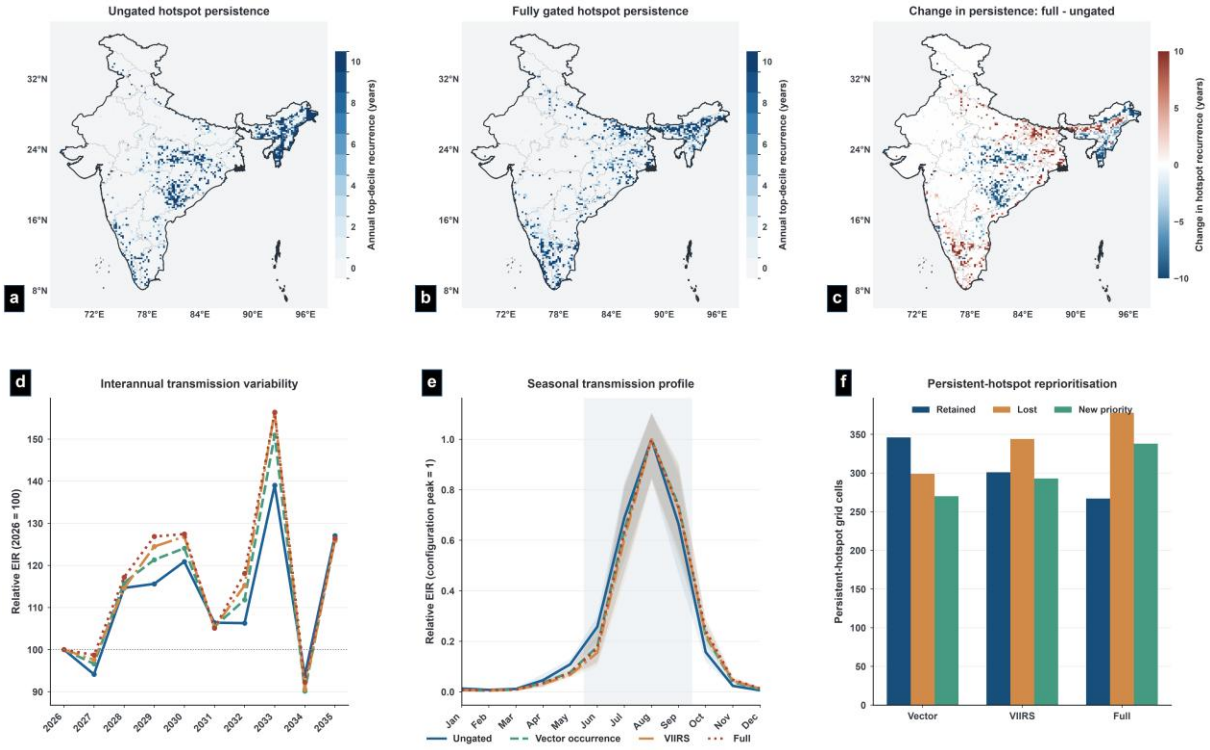


Figure 7 Temporal persistence, interannual variability and seasonal characteristics of mechanistic dengue transmission hotspots under alternative contextual gating configurations*. a,b, Spatial distribution of annual high-EIR hotspot recurrence during 2026–2035 under ungated and fully gated CliMed configurations, respectively. Hotspots were defined independently for each year and configuration as the upper 10% of grid cells with strictly positive annual mean entomological inoculation rate (EIR). Colour intensity represents the number of years, ranging from zero to ten, in which a grid cell satisfied the hotspot criterion. c, Change in hotspot recurrence between fully gated and ungated simulations, calculated as the difference in the number of years classified as a hotspot. Positive values indicate more frequent relative hotspot classification after gating, whereas negative values indicate reduced recurrence. d, Interannual variation in spatially averaged EIR across four configurations: ungated, vector-occurrence gating, VIIRS gating and full gating. Values are normalised independently to the corresponding 2026 annual mean EIR (2026 = 100), allowing comparison of relative temporal variability rather than absolute transmission magnitude. e, Monthly climatological EIR profiles for the same configurations, independently normalised to their respective maximum monthly climatological EIR values. Shaded envelopes indicate the 10th–90th percentile ranges across ten year-specific monthly means, while the grey vertical band denotes the June–September southwest monsoon period. f, Retention, loss and newly prioritised persistent hotspot grid cells under each gating configuration relative to the ungated simulation. Persistent hotspots were defined as locations classified within the annual upper-decile EIR distribution for at least eight of the ten years. All experiments were performed under SSP2-4.5 using daily three-GCM median climate forcing and a common 20-km model grid, with 8,292 common valid grid cells. Vector-occurrence and VIIRS constraints were evaluated individually, while the full configuration incorporated the complete contextual gating framework. Hotspot recurrence and reclassification reflect relative modelled transmission-potential rankings and should not be interpreted as observed vector persistence, human infection recurrence or increasing absolute transmission intensity. Sensitivity analyses using alternative percentile thresholds (85th, 90th and 95th) and persistence criteria (seven, eight and nine years) were conducted to examine the robustness of the geographical reclassification.*

Of the 645 persistent hotspots identified under ungated conditions, only 267 (41.4%) retained their classification after full gating, while 378 (58.6%) were no longer classified as persistent hotspots. Conversely, 338 locations not meeting the ungated persistence criterion became persistently prioritised under full gating, yielding a Jaccard similarity coefficient of 0.272 (Fig. 7f). Vector-occurrence gating alone retained 346 persistent hotspot cells, with 299 lost and 270 newly prioritised locations (Jaccard = 0.378). VIIRS gating retained 301 cells, with 344 lost and 293 newly prioritised locations (Jaccard = 0.321). The corresponding numbers of persistent hotspots

were 616 under vector-occurrence gating and 594 under VIIRS gating. These differences were spatially structured: full gating reduced hotspot recurrence across several previously persistent clusters in northeastern and central India, while increasing relative recurrence in selected locations across the northern plains, eastern regions and southern peninsula (Fig. 7c). The geographical reorganisation was also robust to alternative hotspot definitions. For an eight-year persistence criterion, Jaccard similarity relative to the ungated configuration was 0.323, 0.272 and 0.207 at the 85th, 90th and 95th percentile thresholds, respectively. Persistent-hotspot counts and threshold-sensitivity results are provided in Supplementary Section S6 and Supplementary Tables S6–S7.

Despite the pronounced geographical changes, interannual and seasonal variations in transmission potential remained broadly synchronised across all four configurations (Fig. 7d,e). Relative to their respective 2026 values, mean annual EIR reached its maximum in 2033 under every configuration, increasing by 39.0% in the ungated simulation and 56.3% under full gating, followed by a decline in 2034. The seasonal profiles also retained a common August maximum, although their relative magnitudes differed throughout the year. Under ungated conditions, September and October EIR corresponded to 66.4% and 15.7% of the August climatological maximum, respectively, compared with 72.9% and 24.2% under full gating. Thus, contextual gating modified the relative distribution of transmission potential within the seasonal cycle without shifting the national month of maximum EIR.

Discussion

The geographical expression of dengue transmission potential reflects the combined influence of climatic conditions, vector ecology and human-associated environmental characteristics, rather than climatic suitability alone. Previous studies have demonstrated that climate, urban infrastructure and human mobility contribute differently to dengue emergence[9,10], while recent mechanistic and spatial modelling approaches have highlighted the importance of integrating climate-dependent vector dynamics with ecological suitability and population-related processes[15,17].

Building on these advances, our study demonstrates how climate-conditioned transmission intensity, geographical hotspot prioritisation and temporal persistence respond differently to climate scenarios and contextual constraints within a common mechanistic framework. Across three near-term SSP pathways, simulated entomological inoculation rate (EIR) increased by 13.8–17.8% relative to historical conditions, while the geographical distribution of high-transmission hotspots remained largely conserved (Jaccard similarity: 0.885–0.897). In contrast, full contextual gating under identical SSP2-4.5 climate forcing reduced spatially averaged EIR by 83.4% and substantially reorganised hotspot geography, with only 30.1% overlap between ungated and fully gated hotspot classifications. A corresponding overlap of 27.2% among persistent hotspots further demonstrated that contextual constraints influence not only the relative geographical distribution of transmission potential but also the locations repeatedly prioritised across successive years. These findings distinguish climatic intensification from the ecological and settlement-related organisation of transmission potential.

Experimental and mechanistic studies have established that temperature regulates mosquito survival, development, biting frequency, vector competence and viral incubation through interacting, often nonlinear biological responses, while precipitation and atmospheric moisture

influence vector abundance and the environmental conditions supporting transmission[3–5,15]. Furthermore, daily temperature fluctuations can modify transmission-related biological processes beyond the effects represented by mean temperature alone[12]. Consistent with these findings, our simulations exhibited distinct nonlinear relationships between EIR and temperature, relative humidity and precipitation, with differing responses across historical and near-term climatic conditions. However, spatial-block cross-validation showed that changes in annual-mean meteorological variables provided limited predictive information about the corresponding geographical changes in EIR ($R^2 = -0.071$). This distinction is important because mechanistic transmission potential emerges from the temporal evolution of interacting biological processes, whereas annual climatic summaries compress variations in environmental conditions that may influence those processes differently[23]. The contrast between the fitted climatic relationships and the spatially heterogeneous mechanistic responses therefore highlights the value of retaining daily meteorological variability and process-specific biological responses when evaluating climate-sensitive transmission potential.

The seasonal distribution of transmission potential further demonstrates that climatic intensification does not necessarily produce corresponding shifts in transmission timing or duration. Previous studies have documented the importance of monsoon-associated rainfall, temperature and humidity in shaping dengue transmission across India, alongside substantial regional differences in seasonal occurrence[21,22,24]. Our simulations similarly revealed a pronounced monsoon-associated transmission cycle, but with a disproportionate intensification during its later stages. Although mean EIR increased by 17.7% in August, September exhibited a larger relative increase of 32.8%, accompanied by increases in precipitation and relative humidity. These changes suggest that near-term climatic conditions may strengthen transmission potential towards the latter part of the monsoon season without necessarily shifting its climatological maximum. Indeed, August remained the dominant peak month in both periods, while peak transmission timing was unchanged in 83.0% of valid grid cells. Similarly, the mean seasonal concentration window (L_{80}) remained nearly constant, increasing only from 2.960 to 2.968 months, with no change in 82.8% of grid cells. Rather than indicating a uniform extension of the transmission season, these findings suggest that changes in the magnitude, timing and concentration of transmission potential can follow distinct geographical responses. Such differentiation is particularly relevant in monsoon-dominated environments, where the seasonal coordination of temperature, moisture and rainfall influences multiple components of the vector–host transmission system[3,5].

Previous studies have demonstrated that climate-driven dengue suitability and transmission responses vary geographically, reflecting nonlinear biological processes, regional climatic conditions and natural climate variability[6,25,26]. Recent evidence has also highlighted the influence of large-scale climate variability and teleconnections on heterogeneous dengue transmission patterns[27]. Consistent with this complexity, our near-term simulations exhibited a non-monotonic response across emission pathways, with mean EIR increasing by 14.6%, 17.8% and 13.8% under SSP1-2.6, SSP2-4.5 and SSP5-8.5, respectively. However, differences in transmission intensity were accompanied by substantial geographical agreement: historical-to-future hotspot overlap remained between 0.885 and 0.897, while 714 of the 765 future hotspot cells were shared across all three scenarios. This contrast suggests that the underlying geographical distribution of

favourable transmission conditions can remain relatively stable even when their intensity responds differently to near-term climatic trajectories. The non-monotonic ordering is compatible with the combined influence of regional climate variability and nonlinear biological responses, rather than a simple relationship between emission pathway and transmission magnitude.

The incorporation of ecological occurrence and settlement-related constraints revealed a further distinction between climatically favourable transmission conditions and the geographical organisation of mechanistic transmission potential. Previous investigations have demonstrated that urban infrastructure, human connectivity and environmental barriers influence the spatial expression of dengue transmission and vector establishment, highlighting the importance of ecological and human-associated processes alongside climate[9,10,17]. Our controlled gating experiments extend this perspective by quantifying how individual and combined contextual constraints modify transmission intensity and hotspot prioritisation under identical climatic forcing. Vector-occurrence gating reduced spatially averaged EIR by 65.6%, whereas VIIRS-derived settlement-related gating produced an 81.1% reduction; full contextual gating yielded an 83.4% reduction. Beyond these differences in magnitude, the spatial organisation of transmission potential changed substantially, with hotspot overlap relative to the ungated configuration declining to 0.399, 0.360 and 0.301 under vector-occurrence, VIIRS and full gating, respectively. This geographical reorganisation was also evident in administrative rankings: only five of the ten highest-ranked states and union territories under ungated conditions retained their positions within the top ten following full gating, while several previously lower-ranked regions gained relative prominence. These findings indicate that ecological and settlement-related constraints influence not only the magnitude of simulated transmission potential but also its geographical prioritisation.

The temporal persistence of transmission hotspots provides further evidence that geographical prioritisation and climatic variability represent distinct, although interconnected, characteristics of the transmission landscape. Previous studies have highlighted the importance of climatic variability, environmental suitability and spatial processes in determining the geographical distribution and persistence of Aedes populations and associated transmission potential[5,10,17,26]. Our decade-long analysis showed that ecological and settlement-related constraints substantially reorganised persistent transmission hotspots without fundamentally altering the broader temporal structure of simulated transmission. Although the number of persistent hotspots changed relatively modestly, from 645 under ungated conditions to 605 following full gating, only 267 locations retained their persistent-hotspot classification across both configurations, corresponding to a Jaccard similarity of 0.272. This geographical turnover remained evident across alternative hotspot-percentile and persistence thresholds, indicating that the reorganisation was not dependent on a single classification criterion. In contrast, all four configurations exhibited broadly synchronised interannual variability, including a common maximum in 2033, while their climatological seasonal peaks consistently occurred in August. These contrasting responses suggest that contextual constraints predominantly modify where transmission potential is

repeatedly concentrated, whereas common climatic forcing preserves much of its relative temporal variability.

Global assessments have demonstrated the value of mapping climatic suitability and populations potentially exposed to dengue, while more recent studies have emphasised the importance of ecological conditions, urban infrastructure and spatial connectivity in shaping transmission landscapes[7,9,10]. Our results extend this perspective by showing that locations consistently identified as climatically favourable do not necessarily retain the same geographical priority after ecological occurrence and settlement-related constraints are incorporated. The substantial reclassification of both annual and persistent hotspots suggests that climate-conditioned transmission intensity and contextually constrained transmission potential provide complementary information for spatial prioritisation. In practical terms, identifying locations that remain prominent across climate scenarios, alongside those whose relative importance changes under contextual constraints, could help guide targeted entomological surveillance, environmental assessments and the selection of areas for more detailed local investigations. By retaining these contextual components within a common mechanistic framework, CliMed offers a systematic approach for distinguishing climate-related changes in transmission potential from the geographical reorganisation associated with ecological and human-environmental conditions, complementing existing approaches to climate-sensitive arboviral risk assessment[15,17].

Several considerations define the scope of these findings and provide opportunities for further development of the CliMed framework. First, climate forcing was constructed from the daily median of three CMIP6 models, providing a common climatic representation for the mechanistic experiments but not explicitly quantifying the propagation of individual climate-model uncertainty into transmission estimates. Natural climate variability can substantially influence near-term vector suitability, highlighting the importance of ensemble-based uncertainty assessment in future applications[26]. Second, vector-occurrence, land-use and VIIRS-derived contextual information were held fixed during the near-term experiments to isolate their influence under common climatic conditions. Future changes in vector establishment, settlement characteristics and environmental connectivity could introduce additional spatial dynamics, as demonstrated by studies of vector expansion and dengue emergence[10,17]. The 20-km modelling grid also represents regional transmission heterogeneity rather than fine-scale variations in breeding habitats and human–vector contact. Furthermore, although CliMed incorporates climate-sensitive vector biology and coupled transmission processes, independently evaluating simulated EIR and FOI against spatially and temporally resolved entomological observations would strengthen their quantitative interpretation and applicability across different ecological settings[5,15]. Additional processes, including changing viral serotypes, population immunity and intervention intensity, could also be incorporated when extending the framework towards epidemiological outbreak dynamics, as recent investigations have demonstrated the importance of interactions between climatic variability and serotype competition[28]. Future development could therefore combine time-varying ecological and settlement information, individual climate-model experiments and field-based evaluation to examine how evolving environmental conditions influence transmission potential. Within the present experimental design, however, the consistent contrast between climate-scenario hotspot stability and context-dependent geographical reorganisation provides a basis for understanding how distinct environmental constraints shape the spatial and temporal expression of mechanistic dengue transmission potential.

Methods

Study area

The study covered India, encompassing diverse climatic regimes, land-use characteristics, ecological conditions and human settlement patterns. CliMed simulations were conducted on a common nominal 20-km spatial grid to investigate geographical and temporal variations in mechanistic dengue transmission potential. The same spatial framework was used for historical (2005–2014) and near-term (2026–2035) experiments, enabling direct grid-cell comparisons across climate scenarios and contextual gating configurations. A common analysis mask comprising 8,292 valid grid cells was used for the principal spatial comparisons, with invalid cells excluded rather than assigned zero transmission potential. Analyses of peak transmission timing and seasonal concentration were restricted to 7,634 paired grid cells satisfying the corresponding completeness and positive-EIR criteria. Administrative boundaries were used for geographical visualisation and descriptive aggregation of model outputs at state and union-territory levels. Administrative mean EIR values were calculated from contributing grid cells without population weighting.

Data Sources

Daily meteorological forcing was obtained from three Earth system models participating in the Coupled Model Intercomparison Project Phase 6 (CMIP6): MPI-ESM1-2-LR, MRI-ESM2-0 and ACCESS-ESM1-5[29–32]. The historical experiment covered 2005–2014, while near-term simulations covered 2026–2035 under three Shared Socioeconomic Pathways: SSP1-2.6, SSP2-4.5 and SSP5-8.5, following the Scenario Model Intercomparison Project framework[33]. The meteorological variables comprised daily near-surface air temperature (tas), precipitation (pr) and near-surface specific humidity (huss). These variables were standardised and spatially harmonised before constructing the model forcing. For each experiment, the corresponding daily meteorological fields from the three models were combined using the grid-cell median to produce a common forcing sequence. This sequence was subsequently supplied to CliMed, generating one mechanistic transmission simulation per experimental configuration rather than an ensemble statistic calculated from three independently simulated transmission outputs. Relative humidity was derived from the daily thermodynamic variables, with a reference pressure of 101,325 Pa used where daily surface-pressure information was unavailable. Precipitation was expressed in millimetres per day, and temperature and moisture variables were converted to the units required by the biological formulations. Historical and near-term experiments were analysed separately using consistent spatial harmonisation and temporal aggregation procedures. Additional details of climate-forcing construction and annual-field aggregation are provided in Supplementary Section S1.

Land-use and land-cover (LULC) characteristics were represented using an India-wide processed categorical raster derived from the National Remote Sensing Centre (NRSC), Indian Space Research Organisation (ISRO), IRS-P6 Advanced Wide Field Sensor (AWiFS) land-cover framework[34]. The original AWiFS observations have a nominal spatial resolution of 56 m and were subsequently adapted into model-compatible land-cover products. The processed raster used in CliMed had a spatial resolution of approximately 0.01° (approximately 1 km) and comprised nine land-cover categories within the study domain. Each category was associated with prescribed habitat-productivity and rainfall-response parameters, allowing land-cover heterogeneity to influence mosquito habitat support within the mechanistic framework. Categorical information was transferred to the CliMed analysis grid using nearest-neighbour resampling to preserve discrete

land-cover classes. The same processed LULC representation was retained across the historical and near-term experiments.

Human population information was obtained from the WorldPop gridded population-count dataset for India for 2018, distributed at approximately 1-km spatial resolution[35]. The population raster represents the estimated number of people within individual source grid cells. Population counts were aggregated to the CliMed grid while preserving population totals, and population density was subsequently calculated using the geographical area of each model cell. The resulting fields supplied the population-related quantities required by the vector-to-host and coupled human–vector transmission formulations. Population density and population counts were retained as distinct quantities because they enter different stages of the mechanistic calculations. The 2018 population representation was held fixed across the climate-scenario and contextual-gating experiments, providing a consistent demographic reference for evaluating differences associated with the specified environmental conditions and model configurations.

Species-specific ecological suitability information for Aedes aegypti and Aedes albopictus was obtained from previously developed ecological niche models for India using the maximum entropy (MaxEnt) approach[36]. These models incorporated quality-controlled and spatially thinned species-occurrence records together with approximately 1-km CHELSA bioclimatic predictors to generate continuous geographical suitability surfaces. The resulting species-specific indices were transferred to the common CliMed grid and used to construct ecological occurrence constraints within the mechanistic transmission pathway. The suitability fields were treated as relative indicators of environmental support for vector occurrence, rather than direct measurements of mosquito abundance. These processed ecological layers were maintained consistently across the contextual-gating experiments to allow their influence on simulated transmission potential to be evaluated under common climatic forcing.

Settlement-related environmental characteristics were represented using nighttime-light observations from the Visible Infrared Imaging Radiometer Suite (VIIRS) Day/Night Band, obtained from the Earth Observation Group Annual VIIRS Nighttime Lights product[37]. The annual product is distributed in a geographic coordinate system (EPSG:4326) at approximately 15-arc-second spatial resolution, with radiance expressed in nW cm^{-2} sr^{-1}. VIIRS nighttime-light intensity was used as a remotely sensed indicator of settlement-related environmental characteristics and incorporated into the contextual contact-modification component of CliMed. The processed radiance field was harmonised to the common model grid and retained as a fixed spatial constraint throughout the analysed experiments. Its influence was evaluated separately from species-occurrence constraints and subsequently in combination with them.

All climatic, land-cover, population, vector-suitability and nighttime-light inputs were harmonised to the common CliMed spatial framework before simulation. The climate-scenario analysis compared the historical experiment with three near-term SSP pathways using neutral optional occurrence and VIIRS gates. The contextual-gating analysis was conducted separately under the common SSP2-4.5 climate forcing for 2026–2035, using four configurations: ungated, vector-occurrence gating alone, VIIRS gating alone and full gating. These experiments provided the input configurations for examining climatic changes in transmission potential, geographical hotspot consistency, contextual attenuation and temporal hotspot persistence. Detailed descriptions of the environmental response functions, gate implementation and transmission calculations are provided in the subsequent mechanistic Methods subsections.

CliMed mechanistic modeling framework

CliMed v1.0.0 was implemented as a daily, spatially explicit mechanistic framework linking environmental conditions, mosquito ecology and coupled vector–host infection dynamics to simulate dengue transmission potential across India. The framework represents Aedes aegypti and Aedes albopictus separately, accounting for species-specific biological responses to temperature and the influence of rainfall, relative humidity, land-use characteristics and human population density. Meteorological forcing and ancillary environmental datasets were harmonised to a common nominal 20-km model grid. Within each grid cell, land-use-dependent habitat productivity, antecedent rainfall and moisture suitability were combined with temperature-dependent mosquito development, fecundity, biting activity and mortality to determine dynamic vector-to-host ratios. These quantities subsequently entered species-specific transmission calculations and coupled human–vector infection dynamics, producing daily mechanistic estimates of entomological inoculation rate (EIR) and force of infection (FOI). The biological response functions and compartmental transmission structure follow established mechanistic approaches to Aedes-borne viral transmission[4,38].

The framework additionally incorporates optional ecological-occurrence and settlement-related contextual constraints at defined stages of the mechanistic transmission pathway. These constraints modify the environmental and human-associated conditions governing vector pressure and transmission, rather than operating exclusively as a final spatial multiplier of model outputs. Climate-scenario experiments were performed with optional contextual gates disabled, allowing historical and near-term transmission potential to be compared across SSP1-2.6, SSP2-4.5 and SSP5-8.5. The contextual analysis subsequently evaluated four configurations—ungated, vector-occurrence gating, VIIRS gating and full gating—under identical three-GCM median SSP2-4.5 forcing for 2026–2035. The corresponding habitat, biological, transmission and contextual formulations are described in the following subsections.

LULC-dependent habitat and rainfall response

Land-use and land-cover (LULC) characteristics were incorporated upstream of transmission through class-specific habitat-productivity and rainfall-response parameters. Each land-cover category was assigned a baseline habitat-productivity coefficient and a rainfall half-saturation constant, allowing geographical differences in habitat support and rainfall requirements to be represented within the mechanistic framework. For each grid cell, these parameters were defined as follows:

$$E_0(x) = E_{0,c}, \qquad K(x) = K_c, \qquad c = \mathrm{LULC}(x).$$

Thus, LULC was not applied as a direct multiplier of dengue risk. Instead, it modified the capacity of each grid cell to support mosquito production and the rainfall required for habitat saturation.

The class-specific parameters determine relative habitat productivity and the accumulated rainfall required for habitat support to approach saturation. Recent rainfall was represented using a seven-day accumulation window:

$$P_7(t,x) = \sum_{k=0}^{6} P\,(t-k,x),$$

where $P(t,x)$ is daily precipitation.

Daily precipitation was accumulated over the available preceding days, including the current day. At the beginning of an independently processed simulation period, the available partial window was used without introducing unavailable antecedent rainfall. Rainfall-dependent habitat support was subsequently represented using a saturating response:

$$\sigma_P(t,x) = \frac{P_7(t,x)}{P_7(t,x) + K(x)}.$$

To account for reduced breeding-habitat support under intense precipitation, a separate flushing response was applied using daily rainfall:

$$F(t,x) = \begin{cases} 1, & P(t,x) < P_{\mathrm{thr}}, \\ \exp\left(-k_f\left(P(t,x) - P_{\mathrm{thr}}\right)\right), & P(t,x) \geq P_{\mathrm{thr}}. \end{cases}$$

The resulting effective rainfall suitability was

$$g_P(t,x) = \sigma_P(t,x)\, F(t,x).$$

The model configuration used a seven-day rainfall-memory window, $P_{\mathrm{thr}} = 20\ \mathrm{mm\,day^{-1}}$, and $k_f = 0.1\ \mathrm{mm^{-1}}$.

Relative humidity was represented through a separate moisture-suitability function, allowing atmospheric moisture to influence habitat support independently of the rainfall-response formulation:

$$g_{\mathrm{RH}}(t,x) = \mathrm{clip}\left(\frac{\mathrm{RH}(t,x) - \mathrm{RH}_{\mathrm{min}}}{\mathrm{RH}_{\mathrm{opt}} - \mathrm{RH}_{\mathrm{min}}}, 0{,}1\right).$$

The current species profiles use $\mathrm{RH}_{\mathrm{min}} = 30\%$ and $\mathrm{RH}_{\mathrm{opt}} = 75\%$. Temperature was excluded from the moisture-suitability function because its effects on vector development, fecundity, biting activity and mortality were represented explicitly through the species-specific thermal-response functions described below. The rainfall accumulation and habitat-response structure is consistent with process-based approaches to Aedes population modelling[39,40], while the specific saturation–flushing formulation follows the CliMed implementation.

Temperature-dependent vector biology

Temperature-dependent biting, development, and fecundity were represented using Brière-type nonlinear functions[41]. The formulation was applied separately to biting rate, development rate and fecundity using species-specific coefficients and thermal limits. The functional form follows a Brière-type formulation and its subsequent application in temperature-dependent mosquito-transmission modeling[4]. For a generic biological trait $z_s(T)$ of species s,

$$z_s(T) = \begin{cases} c_s\, T\left(T - T_{\mathrm{min},s}\right)\sqrt{T_{\mathrm{max},s} - T}, & T_{\mathrm{min},s} < T < T_{\mathrm{max},s}, \\ 0, & \text{otherwise.} \end{cases}$$

The species-specific biting rate, fecundity and development rate are denoted by a_s, E_s and ϕ_s, respectively; c_s and the lower and upper thermal limits are trait-specific coefficients.

Experimental evidence further shows that diurnal temperature variation can modify mosquito survival and dengue-virus competence even at the same mean temperature[12].

The temperature–mortality formulation is based on experimentally derived relationships used in dengue-vector population modeling[42]. Multi-setting survival analyses likewise demonstrate strong and species-specific temperature effects on adult *Aedes* survival[43].

Adult mosquito mortality was represented as a fourth-order temperature function:

$$\mu_s(T) = \beta_{0,s} + \beta_{1,s}T + \beta_{2,s}T^2 + \beta_{3,s}T^3 + \beta_{4,s}T^4.$$

A lower mortality bound was imposed:

$$\tilde{\mu}_s(T) = \max(\mu_s(T), \mu_{\min}),$$

with $\mu_{\min} = 0.05\ \text{day}^{-1}$. Species-specific mortality coefficients were retained in the CliMed parameter profiles. For *Ae. albopictus*, temperature was restricted to the fitted 15–35 °C interval when evaluating the mortality polynomial to avoid extrapolation outside the supported temperature range.

The temperature-dependent extrinsic incubation period was represented using a degree-day formulation:

$$\text{EIP}_s(T) = \frac{D_s}{T - T_{0,s}}, \qquad T > T_{0,s},$$

where D_s is the species-specific degree-day requirement and $T_{0,s}$ is the lower temperature threshold. In the operational implementation, EIP was bounded between 3 and 30 days:

$$\widetilde{\text{EIP}}_s(T) = \text{clip}(\text{EIP}_s(T), 3, 30).$$

Temperature-dependent survival through the EIP was calculated as

$$P_{\text{EIP},s}(T) = \exp\left(-\tilde{\mu}_s(T)\, \widetilde{\text{EIP}}_s(T)\right).$$

This formulation couples temperature-dependent viral development with adult mosquito survival, consistent with established dengue vectorial-capacity approaches[44]. Temperature constraints on persistence and competence of both vector species provide additional support for coupling viral development with mosquito survival[13].

Dynamic vector-to-host ratio

CliMed does not prescribe a fixed mosquito-to-human ratio. Instead, daily vector pressure is derived from LULC-dependent habitat productivity, mosquito thermal traits, rainfall support, mortality and local host density. For species s,

$$m_s(t,x) = \frac{E_0(x)\, E_s(T)\, \phi_s(T)\, \sigma_P(t,x)\, F(t,x)}{H_{\text{eff}}(x)\, \tilde{\mu}_s(T)}.$$

Here, $H_{\text{eff}}(x)$ represents local human population density, with a small positive lower bound applied only to avoid numerical instability in cells with zero population. The numerator represents relative mosquito production pressure, which increases under favorable habitat productivity, fecundity, development, and rainfall conditions. The denominator reduces the vector-to-host ratio where adult mortality or host density is high. Accordingly, the resulting quantity is interpreted as a model-derived vector-to-host ratio rather than a direct observation of mosquito abundance.

Contextual ecological constraints

The environmental and biological calculations described above, including LULC-dependent habitat effects, form the core mechanistic model. In the fully gated configuration, additional ecological-occurrence and human-contextual information was incorporated through bounded soft gates rather than binary exclusion masks. These gates act at distinct positions within the mechanistic pathway.

For each species, the relative ecological-suitability index $O_s(x)$ was first normalized between lower and upper occurrence limits:

$$O'_s(x) = \mathrm{clip}\left(\frac{O_s(x) - O_{\mathrm{low},s}}{O_{\mathrm{high},s} - O_{\mathrm{low},s}}, 0{,}1\right).$$

The corresponding occurrence gate was

$$G_{\mathrm{occ},s}(x) = f_{\mathrm{occ}} + (1 - f_{\mathrm{occ}})\left(\frac{1}{1 + \exp\{-\kappa_{\mathrm{occ},s}(O'_s(x) - 0.5)\}}\right).$$

Here, f_{occ} is the gate's lower bound and $\kappa_{occ,s}$ controls its steepness.

Occurrence therefore modifies vector pressure before transmission is calculated. Where the optional population-pressure modifier was enabled, population density was additionally represented relative to a reference density H_{ref}:

$$G_{\mathrm{pop}}(x) = \max\left(G_{\min}, \left\{\mathrm{clip}\left(\frac{H(x)}{H_{\mathrm{ref}}}, 0, G_{\max}\right)\right\}^{\alpha}\right).$$

The contextually modified vector-to-host ratio was consequently

$$\widetilde{m}_s(t,x) = m_s(t,x)\, G_{\mathrm{occ},s}(x)\, G_{\mathrm{pop}}(x).$$

Settlement intensity was transformed into a bounded human–vector contact function:

$$G_{V,s}(x) = f_{V,s} + \left(1 - f_{V,s}\right)\left(\frac{1}{1 + \exp\left\{-\kappa_{V,s}\dfrac{V(x) - V_0}{w_V}\right\}}\right),$$

where $V(x)$ is the settlement-intensity field, V_0 is the configured threshold centre, $f_{V,s}$ is the species-specific lower bound, and w_V is determined from the spatial spread of the settlement field. The width used in the implementation was

$$w_V = \max\left(\frac{Q_{0.90}(V) - Q_{0.10}(V)}{6}, 0.1|V_0|, 10^{-6}\right).$$

The parameter $\kappa_{V,s}$ controls the steepness of the settlement response.

This term is interpreted as a settlement/contact modifier rather than a mosquito physiological response.

Population context and population at risk

Population contributes to CliMed at two distinct stages. Population density influences the vector-to-host relationship upstream, whereas population per grid cell determines the population over which the resulting infection probability is expressed downstream.

Population density $H(x)$ was normalized relative to its 90th percentile H_{90}:

$$D_{\mathrm{norm}}(x) = \mathrm{clip}\left(\frac{\ln\left(1 + H(x)\right)}{\ln(1 + H_{90})}, 0{,}1\right).$$

When population-context gating was enabled together with settlement information, the urbanicity index was

$$U(x) = 0.55\, G_V(x) + 0.45\, D_{\mathrm{norm}}(x).$$

Cells were categorized as

$$C(x) = \begin{cases} \text{rural}, & U(x) < 0.33, \\ \text{peri-urban}, & 0.33 \le U(x) < 0.66, \\ \text{urban}, & U(x) \ge 0.66. \end{cases}$$

The class-specific exposed fraction was derived from contact and density terms. For urban cells,

$$f_{\text{exp}}^{\text{urban}}(x) = f_{\text{min}}^{\text{urban}} + \left(f_{\text{max}}^{\text{urban}} - f_{\text{min}}^{\text{urban}}\right) G_V(x)(1 - \exp\{-2D_{\text{norm}}(x)\}).$$

For peri-urban cells,

$$f_{\text{exp}}^{\text{peri}}(x) = f_{\text{min}}^{\text{peri}} + \left(f_{\text{max}}^{\text{peri}} - f_{\text{min}}^{\text{peri}}\right)\left(0.5G_V(x) + 0.5D_{\text{norm}}(x)\right).$$

For rural cells,

$$f_{\text{exp}}^{\text{rural}}(x) = f_{\text{min}}^{\text{rural}} + \left(f_{\text{max}}^{\text{rural}} - f_{\text{min}}^{\text{rural}}\right)(0.35G_V(x) + 0.65\{1 - D_{\text{norm}}(x)\}).$$

The configured exposed-fraction intervals were 0.03–0.18 for urban cells, 0.05–0.28 for peri-urban cells and 0.08–0.40 for rural cells. The corresponding susceptible fractions were 0.12, 0.16 and 0.22, respectively. These exposure and susceptibility values are configuration assumptions rather than measured epidemiological fractions. Their ordering across settlement classes is not presented as empirical evidence of greater rural exposure. Context-specific population fractions and principal fixed configuration values are summarised in Supplementary Section S7 and Supplementary Tables S8–S9.

The population base supplied to the human transmission model was

$$N_{\text{risk}}(x) = N_{\text{cell}}(x)\, f_{\text{exp}}(x)\, f_{\text{sus}}(x).$$

Thus, population density contributes upstream to vector-to-host interactions, whereas $N_{\text{risk}}(x)$ determines the population over which infection probability is expressed.

Species-specific transmission potential

For each species, CliMed calculates an environmentally and contextually conditioned potential EIR:

$$\text{EIR}_s^{\text{pot}}(t,x) = a_s(T)\, \tilde{m}_s(t,x)\, P_{\text{EIP},s}(T)\, g_{\text{RH}}(t,x)\, G_{V,s}(x).$$

The corresponding potential human force of infection is

$$\lambda_{h,s}^{\text{pot}}(t,x) = b_{vh,s}\, \text{EIR}_s^{\text{pot}}(t,x),$$

where $b_{vh,s}$ is the vector-to-human transmission probability.

The vector-side infection-contact potential was represented as

$$\lambda_{v,s}^{\text{pot}}(t,x) = c_v\, a_s(T)\, G_{V,s}(x)\, g_{\text{RH}}(t,x),$$

where c_v is the configured vector-contact scaling term. These quantities represent environmental and ecological transmission potential before feedback from dynamically evolving human and vector infection states.

Coupled human–vector infection dynamics

Humans were represented by susceptible, exposed, and infectious counts per model cell,

$$S_h(t,x), \qquad E_h(t,x), \qquad I_h(t,x),$$

whereas each vector species was represented by susceptible, exposed, and infectious fractions,

$$S_{v,s}(t,x), \qquad E_{v,s}(t,x), \qquad I_{v,s}(t,x),$$

with

$$S_{v,s}(t,x) + E_{v,s}(t,x) + I_{v,s}(t,x) = 1.$$

The general host–vector compartmental formulation follows established mechanistic dengue models[38].

Daily human progression probabilities were

$$p_{E_h \to I_h} = 1 - \exp\left(-\frac{1}{\tau_{\mathrm{IIP}}}\right),$$

and

$$p_{I_h \to R_h} = 1 - \exp\left(-\frac{1}{\tau_{\mathrm{inf}}}\right),$$

with $\tau_{\mathrm{IIP}} = 6.0$ days and $\tau_{\mathrm{inf}} = 5.9$ days in the analysed configuration. Recovery removes individuals from the infectious compartment; recovered individuals are not returned to susceptibility within an annual experiment. The recovery term denotes daily removals; no separate recovered compartment was propagated.

The dynamically simulated infectious-vector fraction modified potential human transmission according to

$$M_{v,s}(t,x) = \mathrm{clip}\left(\frac{I_{v,s}(t,x)}{I_{v,s}^{\mathrm{ref}}}, 0, M_{v,\max}\right).$$

Here, $I_{v,s}^{ref}$ is the configured infectious-vector reference fraction and $M_{v,max}$ is the upper modulation bound.

The realized species-specific human force of infection was

$$\lambda_{h,s}(t,x) = \lambda_{h,s}^{\mathrm{pot}}(t,x)\, M_{v,s}(t,x).$$

The two species-specific forces of infection were combined additively, without applying species weights to the dynamic transmission contributions:

$$\lambda_h(t,x) = \lambda_{h,\mathrm{aeg}}(t,x) + \lambda_{h,\mathrm{alb}}(t,x).$$

Realized EIR uses modulation relative to a configured infectious-vector reference prevalence and is interpreted as a model transmission quantity rather than an independently calibrated infectious-bite rate. The combined EIR was calculated as

$$\mathrm{EIR}(t,x) = \mathrm{EIR}_{\mathrm{aeg}}^{\mathrm{pot}}(t,x) M_{v,\mathrm{aeg}}(t,x) + \mathrm{EIR}_{\mathrm{alb}}^{\mathrm{pot}}(t,x) M_{v,\mathrm{alb}}(t,x).$$

The daily probability of infection was

$$p_h(t,x) = 1 - \exp\big(-\lambda_h(t,x)\big).$$

New human exposures were

$$\Delta E_h(t,x) = \min\big(S_h(t,x), S_h(t,x)\, p_h(t,x)\big).$$

Human states were updated as

$$S_h(t+1,x) = S_h(t,x) - \Delta E_h(t,x),$$

$$\Delta I_h(t,x) = \min\big(E_h(t,x), E_h(t,x)\, p_{E_h \to I_h}\big),$$

$$\Delta R_h(t,x) = \min\big(I_h(t,x), I_h(t,x)\, p_{I_h \to R_h}\big),$$

$$E_h(t+1,x) = E_h(t,x) + \Delta E_h(t,x) - \Delta I_h(t,x),$$

and

$$I_h(t+1,x) = I_h(t,x) + \Delta I_h(t,x) - \Delta R_h(t,x).$$

The resulting quantity represents daily new human exposures within each model cell. Because the human compartments are expressed as counts, this quantity is already a cell-level count and is not multiplied again by population.

Vector infection dynamics

The contemporaneous infectious-human fraction was

$$i_h(t,x) = \frac{I_h(t,x)}{N_{\text{risk}}(x)}.$$

Its modulation of vector infection was represented as

$$M_h(t,x) = \text{clip}\left(\frac{i_h(t,x)}{i_h^{\text{ref}}}, 0, M_{h,\max}\right).$$

Here, i_h^{ref} is the configured infectious-human reference fraction and $M_{h,max}$ is the upper modulation bound.

The realized force of infection acting on susceptible vectors was

$$\lambda_{v,s}(t,x) = \lambda_{v,s}^{\text{pot}}(t,x)\, M_h(t,x),$$

giving daily vector infection probability

$$p_{v,s}(t,x) = 1 - \exp\left(-\lambda_{v,s}(t,x)\right).$$

Progression from exposed to infectious vectors was governed by the temperature-dependent EIP:

$$p_{E_v \to I_v,s}(t,x) = 1 - \exp\left(-\frac{1}{\widetilde{\text{EIP}}_s(T)}\right).$$

Adult-vector mortality probability was

$$p_{\text{death},s}(t,x) = 1 - \exp\left(-\tilde{\mu}_s(T)\right).$$

New exposed and infectious vector fractions were

$$\Delta E_{v,s}(t,x) = \min\left(S_{v,s}(t,x), S_{v,s}(t,x)\, p_{v,s}(t,x)\right),$$

and

$$\Delta I_{v,s}(t,x) = \min\left(E_{v,s}(t,x), E_{v,s}(t,x)\, p_{E_v \to I_v,s}(t,x)\right).$$

Mortality was applied to the three vector compartments and the corresponding losses were returned to the susceptible compartment, after which the vector fractions were normalized so that

$$S_{v,s} + E_{v,s} + I_{v,s} = 1.$$

Configured seed fractions initialized exposed and infectious human counts as fractions of the population at risk; susceptible counts were the remainder. For each vector species, susceptible fractions were initialized as one minus the exposed and infectious seed fractions. In the analysed configuration, epidemic states were reset at calendar-year boundaries, allowing annual climate-conditioned transmission experiments to be compared without progressive multi-year depletion of susceptible hosts. These resets reinitialize human and vector states and do not represent continuously evolving immunity across years.

Ungated and fully gated configurations

The ungated experiment retained the core climate–LULC–population–vector transmission mechanism while neutralizing the optional occurrence and settlement/context constraints. Population density remained part of the basic vector-to-host calculation and was therefore not removed from the biological transmission backbone.

The fully gated configuration activated species-specific vector-occurrence constraints, population-pressure modification where applicable, VIIRS-derived settlement/contact modification, population-context classification, exposed-population adjustment and susceptible-population adjustment. Because these components operate at different stages of the transmission pathway, the gated configuration is not equivalent to applying a single multiplicative risk mask to the final EIR field.

Annual and seasonal transmission analyses

Daily EIR and FOI outputs were aggregated to annual mean fields for the reference and near-term periods. For variable X, near-term change was calculated as

$$\Delta X(x) = \overline{X}_{\text{future}}(x) - \overline{X}_{\text{historical}}(x).$$

Monthly climatologies were calculated from year-specific monthly means so that each year contributed equally to the seasonal climatology. The 10th–90th percentile range across year-specific monthly means was used to characterize interannual variability and was not interpreted as a confidence interval.

For each grid cell, peak transmission month was identified as

$$M_{\text{peak}}(x) = \underset{m\in\{1,\ldots,12\}}{\arg\max}\ \text{EIR}_m(x).$$

Reference-to-near-term timing changes were calculated using the shortest circular displacement on the 12-month calendar.

Seasonal concentration was quantified using L_{80}, defined as the minimum number of contiguous calendar months containing at least 80% of annual climatological EIR:

$$L_{80}(x) = \min\left\{L: \max_{m\in\{1,\ldots,12\}} \frac{\sum_{j=0}^{L-1} \text{EIR}_{((m+j-1) \bmod 12)+1}\,(x)}{\sum_{q=1}^{12} \text{EIR}_q\,(x)} \geq 0.80\right\}.$$

Contiguity was evaluated circularly across December–January. L_{80} therefore represents a relative measure of seasonal concentration and not an epidemiological transmission threshold.

Climate–EIR response analysis

Grid-cell EIR values were first summarised across 20 equal-frequency classes of near-surface air temperature, relative humidity and precipitation. Median EIR within each class provided an empirical description of the marginal climate-response structure independently of the fitted statistical model.

Nonlinear conditional relationships were subsequently represented using additive spline–ridge regression. Each meteorological predictor was transformed independently using a cubic spline basis of degree three with six knots and no bias term, after which the transformed predictor matrices were combined and fitted using ridge regression with a regularisation parameter of 10. Separate models were fitted for historical EIR, near-term EIR and near-term-minus-historical EIR (ΔEIR). Conditional response curves were evaluated by varying one meteorological predictor across its sampled range while holding the remaining predictors at their median values.

The ability of changes in annual-mean meteorological conditions to predict spatial variation in ΔEIR was evaluated using five-fold grouped cross-validation. Grid cells were assigned to non-overlapping 3° × 3° geographical blocks, and entire spatial blocks were retained within either the training or validation subset to reduce optimistic predictive estimates caused by spatial dependence between neighbouring cells[45]. Predictive performance was quantified using cross-validated R^2.

The contribution of each meteorological variable to out-of-block predictive performance was examined using a drop-one procedure. For each predictor, the model was refitted without that variable using the same spatial cross-validation structure, and the change in predictive performance was calculated as $R^2_{full} - R^2_{reduced}$. Consequently, a negative value indicates that removing the predictor improved out-of-block prediction. For descriptive spatial attribution, the full additive model was also fitted to all valid grid cells, centred fitted contributions were calculated for the individual meteorological components, and each grid cell was assigned the variable with the largest absolute fitted contribution. Spatial residuals were calculated as mechanistically simulated ΔEIR minus cross-validated predicted ΔEIR. These statistical analyses were used to characterise CliMed outputs and were not interpreted as independent causal attribution or validation of the mechanistic model.

Cross-scenario hotspot consistency

Period-mean EIR and FOI fields were calculated from equal-weight annual means for the historical period (2005–2014) and each near-term SSP experiment (2026–2035). Spatial means were calculated as unweighted means across the common valid model grid. Percentage change in a spatially averaged transmission metric was calculated from the ratio of the corresponding period means rather than from the mean of grid-cell percentage changes.

For each period and scenario, high-transmission hotspots were defined independently as grid cells belonging to the upper 10% of strictly positive period-mean EIR values. Grid cells with zero EIR were not eligible for hotspot classification, whereas values equal to the percentile threshold were retained. Historical-to-near-term hotspot agreement was quantified using the Jaccard similarity coefficient, defined as the size of the intersection divided by the size of the union of the corresponding hotspot sets. Pairwise Jaccard similarities were additionally calculated among the three near-term SSP hotspot distributions. Cross-scenario consensus was determined by counting, for each grid cell, the number of near-term SSP experiments in which it satisfied the hotspot criterion. All scenario comparisons used the same finite spatial comparison domain of 8,292 valid grid cells.

Contextual gating and spatial reprioritisation

The effects of contextual constraints were evaluated under identical three-GCM median SSP2-4.5 forcing for 2026–2035. Four model configurations were compared: ungated, vector-occurrence gating, VIIRS-related gating and full contextual gating. Spatial attenuation was calculated relative to the ungated simulation as ungated minus gated EIR, such that positive values represent lower transmission potential following application of the selected contextual constraints.

For each configuration, hotspots were defined independently as the upper 10% of strictly positive period-mean EIR values. Spatial overlap with the ungated hotspot distribution was quantified using the Jaccard coefficient, and hotspot cells were classified as retained, lost from the ungated distribution or newly prioritised under the gated configuration. Grid-cell EIR rank agreement was additionally quantified using Spearman's rank correlation coefficient. For descriptive

administrative comparisons, EIR was averaged across contributing model grid cells within each state or union territory without population weighting, and the resulting administrative means were ranked independently for each model configuration. These comparisons represent changes in relative modelled transmission-potential prioritisation rather than observed dengue burden.

Temporal persistence of transmission hotspots

Temporal hotspot persistence was evaluated annually across the SSP2-4.5 period 2026–2035. Within each year and model configuration, hotspots were defined independently as the upper 10% of grid cells with strictly positive annual mean EIR. For each grid cell, hotspot recurrence was calculated as the number of years in which the annual hotspot criterion was satisfied. A persistent hotspot was defined a priori as a location classified as an annual hotspot in at least eight of the ten years.

Persistent-hotspot distributions under each contextual configuration were compared with the ungated distribution using retained, lost and newly prioritised grid-cell counts and the Jaccard similarity coefficient. Robustness was assessed using alternative hotspot thresholds corresponding to the upper 15%, 10% and 5% of positive EIR values and alternative persistence requirements of at least seven, eight or nine years.

Interannual EIR variability was compared among configurations after normalising each annual spatial mean independently to its corresponding 2026 value, with 2026 assigned an index of 100. Monthly climatologies were calculated by first averaging daily EIR within each calendar month and year and subsequently calculating equal-weight means across the ten years. The 10th–90th percentile range across year-specific monthly means was used to describe interannual variability. To compare seasonal timing independently of absolute transmission magnitude, each configuration's monthly climatology was normalised to its own maximum monthly EIR. These normalised comparisons describe relative temporal structure; absolute attenuation was evaluated separately using the unnormalised simulations.

Data availability

The input datasets are available from the sources cited in the Methods section. Processed model outputs and source data underlying the figures, tables, and statistical analyses will be supplied in a ZIP archive accompanying the submission for confidential peer review. Public archival details will be included in the non-anonymized manuscript before publication.

Code availability

The CliMed source code, run configurations, and analysis scripts supporting this study will be supplied in a ZIP archive accompanying the submission for confidential peer review. This includes the workflows for climate and ancillary-data preprocessing, species-specific transmission calculations, and combined contextual transmission analysis. Public archival details and applicable license terms will be included in the non-anonymized manuscript before publication.

Acknowledgements

This research received no specific funding.

Author contributions

The first author conceived the study, developed CliMed, designed and performed the computational experiments, assembled and processed the datasets, conducted the analyses, generated the figures and tables, interpreted the results, and drafted the manuscript. The second

author supervised the research and reviewed and corrected the manuscript. Both authors approved the final manuscript.

Competing interests

The authors hold copyright in CliMed. They declare no patent or commercial licensing interests and no other competing interests relevant to this work.

References

1. Bhatt, S. et al. The global distribution and burden of dengue. *Nature* **496**, 504–507 (2013).
2. Guzman, M. G., Gubler, D. J., Izquierdo, A., Martinez, E. & Halstead, S. B. Dengue infection. *Nat. Rev. Dis. Primers* **2**, 16055 (2016).
3. Morin, C. W., Comrie, A. C. & Ernst, K. Climate and dengue transmission: evidence and implications. *Environ. Health Perspect.* **121**, 1264–1272 (2013).
4. Mordecai, E. A. et al. Detecting the impact of temperature on transmission of Zika, dengue, and chikungunya using mechanistic models. *PLoS Negl. Trop. Dis.* **11**, e0005568 (2017).
5. Caldwell, J. M. et al. Climate predicts geographic and temporal variation in mosquito-borne disease dynamics on two continents. *Nat. Commun.* **12**, 1233 (2021).
6. Ryan, S. J., Carlson, C. J., Mordecai, E. A. & Johnson, L. R. Global expansion and redistribution of Aedes-borne virus transmission risk with climate change. *PLoS Negl. Trop. Dis.* **13**, e0007213 (2019).
7. Messina, J. P. et al. The current and future global distribution and population at risk of dengue. *Nat. Microbiol.* **4**, 1508–1515 (2019).
8. Kraemer, M. U. G. et al. Past and future spread of the arbovirus vectors Aedes aegypti and Aedes albopictus. *Nat. Microbiol.* **4**, 854–863 (2019).
9. Gibb, R. et al. Interactions between climate change, urban infrastructure and mobility are driving dengue emergence in Vietnam. *Nat. Commun.* **14**, 8179 (2023).
10. Harish, V. et al. Human movement and environmental barriers shape the emergence of dengue. *Nat. Commun.* **15**, 4205 (2024).
11. Reiner, R. C. et al. A systematic review of mathematical models of mosquito-borne pathogen transmission: 1970–2010. *J. R. Soc. Interface* **10**, 20120921 (2013).
12. Lambrechts, L. *et al.* Impact of daily temperature fluctuations on dengue virus transmission by Aedes aegypti. *Proc. Natl. Acad. Sci. U. S. A.* **108**, 7460–7465 (2011).
13. Brady, O. J. et al. Global temperature constraints on Aedes aegypti and Ae. albopictus persistence and competence for dengue virus transmission. *Parasit. Vectors* **7**, 338 (2014).

14. Mordecai, E. A. et al. Thermal biology of mosquito-borne disease. *Ecol. Lett.* **22**, 1690–1708 (2019).

15. Zardini, A. et al. Estimating the potential risk of transmission of arboviruses in the Americas and Europe: a modelling study. *Lancet Planet. Health* **8**, e30–e40 (2024).

16. Smith, D. L. et al. Ross, Macdonald, and a theory for the dynamics and control of mosquito-transmitted pathogens. *PLoS Pathog.* **8**, e1002588 (2012).

17. Barman, S. et al. A climate and population dependent diffusion model forecasts the spread of Aedes albopictus mosquitoes in Europe. *Commun. Earth Environ.* **6**, 276 (2025).

18. Chakravarti, A., Arora, R. & Luxemburger, C. Fifty years of dengue in India. *Trans. R. Soc. Trop. Med. Hyg.* **106**, 273–282 (2012).

19. Ganeshkumar, P. *et al.* Dengue infection in India: a systematic review and meta-analysis. *PLoS Negl. Trop. Dis.* **12**, e0006618 (2018).

20. Murhekar, M. V et al. Burden of dengue infection in India, 2017: a cross-sectional population based serosurvey. *Lancet Glob. Health* **7**, e1065–e1073 (2019).

21. Mutheneni, S. R., Morse, A. P., Caminade, C. & Upadhyayula, S. M. Dengue burden in India: recent trends and importance of climatic parameters. *Emerg. Microbes Infect.* **6**, e70 (2017).

22. Singh, P. S. & Chaturvedi, H. K. Temporal variation and geospatial clustering of dengue in Delhi, India 2015–2018. *BMJ Open* **11**, e043848 (2021).

23. Paaijmans, K. P. et al. Influence of climate on malaria transmission depends on daily temperature variation. *Proc. Natl Acad. Sci. USA* **107**, 15135–15139 (2010).

24. Sophia, Y. *et al.* Dengue dynamics, predictions, and future increase under changing monsoon climate in India. *Sci. Rep.* **15**, 1637 (2025).

25. Colón-González, F. J. et al. Projecting the future incidence and burden of dengue in Southeast Asia. *Nat. Commun.* **14**, 5439 (2023).

26. Kaye, A. R. et al. The impact of natural climate variability on the global distribution of Aedes aegypti: a mathematical modelling study. *Lancet Planet. Health* **8**, e1079–e1087 (2024).

27. Tian, Y. et al. Rising dengue risk with increasing El Niño–Southern Oscillation amplitude and teleconnections. *Nat. Commun.* **16**, 8629 (2025).

28. Finch, E. *et al.* Climate variation and serotype competition drive dengue outbreak dynamics in Singapore. *Nat. Commun.* **16**, 11364 (2025).

29. Eyring, V. et al. Overview of the Coupled Model Intercomparison Project Phase 6 (CMIP6) experimental design and organization. *Geosci. Model Dev.* **9**, 1937–1958 (2016).

30. Mauritsen, T. et al. Developments in the MPI-M Earth System Model version 1.2 (MPI-ESM1.2) and its response to increasing CO2. *J. Adv. Model. Earth Syst.* **11**, 998–1038 (2019).

31. Yukimoto, S. et al. The Meteorological Research Institute Earth System Model Version 2.0, MRI-ESM2.0: Description and Basic Evaluation of the Physical Component. *J. Meteorol. Soc. Japan* **97**, 931–965 (2019).

32. Ziehn, T. et al. The Australian Earth System Model: ACCESS-ESM1.5. *J. South. Hemisph. Earth Syst. Sci.* **70**, 193–214 (2020).

33. O'Neill, B. C. et al. The Scenario Model Intercomparison Project (ScenarioMIP) for CMIP6. *Geosci. Model Dev.* **9**, 3461–3482 (2016).

34. Gharai, B., Rao, P. V. N. & Dutt, C. B. S. Mesoscale model compatible IRS-P6 AWiFS-derived land use/land cover of Indian region. *Curr. Sci.* **115**, 2301–2306 (2018).

35. WorldPop & Center for International Earth Science Information Network (CIESIN). Global High Resolution Population Denominators Project: The spatial distribution of population in 2018 India. https://doi.org/10.5258/SOTON/WP00670 (2018) doi:10.5258/SOTON/WP00670.

36. Peri, S. H. P. Dengue vector niche modeling with future SSP climatic scenarios over India using the machine learning-based MaxEnt model. *Int. J. Biometeorol.* **70**, 125 (2026).

37. Elvidge, C. D., Zhizhin, M., Ghosh, T., Hsu, F.-C. & Taneja, J. Annual Time Series of Global VIIRS Nighttime Lights Derived from Monthly Averages: 2012 to 2019. *Remote Sens. (Basel).* **13**, 922 (2021).

38. Medeiros, L. C. de C. et al. Modeling the Dynamic Transmission of Dengue Fever: Investigating Disease Persistence. *PLoS Negl. Trop. Dis.* **5**, e942 (2011).

39. Cailly, P. et al. A climate-driven abundance model to assess mosquito control strategies. *Ecol. Modell.* **227**, 7–17 (2012).

40. Tran, A. et al. A Rainfall- and Temperature-Driven Abundance Model for Aedes albopictus Populations. *Int. J. Environ. Res. Public Health* **10**, 1698–1719 (2013).

41. Brière, J.-F., Pracros, P., Le Roux, A.-Y. & Pierre, J.-S. A Novel Rate Model of Temperature-Dependent Development for Arthropods. *Environ. Entomol.* **28**, 22–29 (1999).

42. Yang, H. M., Macoris, M. L. G., Galvani, K. C., Andrighetti, M. T. M. & Wanderley, D. M. V. Assessing the effects of temperature on the population of Aedes aegypti, the vector of dengue. *Epidemiol. Infect.* **137**, 1188–1202 (2009).

43. Brady, O. J. et al. Modelling adult Aedes aegypti and Aedes albopictus survival at different temperatures in laboratory and field settings. *Parasit. Vectors* **6**, 351 (2013).

44. Liu-Helmersson, J., Stenlund, H., Wilder-Smith, A. & Rocklöv, J. Vectorial Capacity of Aedes aegypti: Effects of Temperature and Implications for Global Dengue Epidemic Potential. *PLoS One* **9**, e89783 (2014).

45. Roberts, D. R. et al. Cross-validation strategies for data with temporal, spatial, hierarchical, or phylogenetic structure. *Ecography* **40**, 913–929 (2017).

Supplementary Files

This is a list of supplementary files associated with this preprint. Click to download.

- CliMedNatCommsSupplementaryInformationFinal.pdf
- CliMedResultsallwithplotingfiles.zip
- CliMedSourceCodeV1.zip
- CliMedNatCommsSupplementaryInformationFinal.pdf